

# Ice condensation as a planet formation mechanism

*Katrin Ros*

---

Lund Observatory  
Lund University



2012-EXA61

Degree project of 60 higher education credits (for a degree of Master)  
May 2012

Lund Observatory  
Box 43  
SE-221 00 Lund  
Sweden

## Abstract

In models of dust growth in protoplanetary discs focus is typically on coagulation, a mechanism which unfortunately seems incapable of forming particles larger than centimeters. The main reasons for this are that collisions between larger particles lead to bouncing or fragmentation rather than sticking, and that particles approaching meter-sizes drift radially inwards in the disc due to interaction with the surrounding gas. The concept of ice lines is often overlooked, but is of great importance as particles can grow also by condensation. As a volatile species drifts in towards the central star, it sublimates as it passes the ice line of that particular species. The vapour diffuses back across the ice line and condenses onto existing dust grains, leading to significant growth.

We model the dynamical behaviour of ice particles close to the water ice line, around 3 AU from the central star. Ice particles and water vapour move in a damped random walk, due to turbulence in the gas, gravity towards the midplane and radial drift towards the central star. The ice line is curved, and we therefore model it as being composed of the radial ice line, separating the hot region close to the star from the outer cold region of the disc, and the atmospheric ice line, separating the hot midplane and the colder outer layers. Main focus is on diffusion over the atmospheric ice line, but we also look at the effect of including the radial ice line. Condensation and sublimation are modelled with a Monte Carlo approach. The effect of varying the turbulent alpha value, as well as the distance from the atmospheric ice line to the midplane, is investigated. Our results indicate that, with a turbulent  $\alpha$ -value of 0.01, growth from millimeter-sized to at least decimeter-sized particles is possible in the vicinity of the ice line, on a time scale of 1 000 years.

The resulting particle layer may be dense enough to be sensitive to dynamical instabilities, such as the streaming instability, which causes further growth into planetesimals. From planetesimals to planets growth is possible via gravitational interactions.



## Populärvetenskaplig sammanfattning

Planetsystem bildas tillsammans med en stjärna då ett gas- och stoftmoln kollapsar av sin egen gravitation. Ur denna kollaps bildas en protostjärna, omgiven av en så kallad protoplanetär skiva bildad av det överblivna materialet. Då stoftkorn i skivan kolliderar bildas större och större partiklar. När kilometerstora is- och stenblock, eller planetesimaler, har bildats, kan dessa kollidera med varandra och slutligen bilda planeter.

Kollisioner som tillväxtmekanism fungerar dock bara för små partiklar, som hålls samman av van der Waals-krafter, och för mycket stora is- och stenblock, där gravitationen mellan blocken är stark. Då partiklar i storlekar mellan stoftkorn och planetesimaler kolliderar studsar de istället mot varandra, eller bryts sönder vid tillräckligt höga hastigheter. Planetesimaler kan dock bildas av decimeterstora is- och stenblock, då dessa klumpas ihop genom dynamiska instabiliteter som uppkommer genom växelverkan med gas i den protoplanetära skivan.

Detta betyder att vi kan förklara hur små stoftkorn, upp till några millimeter i storlek, och stenblock större än en kilometer, växer genom kollisioner, och hur decimeterstora is- och stenblock växer till kilometerstora planetesimaler genom dynamiska instabiliteter. Hur partiklar i den protoplanetära skivan växer från millimeter till decimeter kan däremot inte förklaras med någon av dessa modeller.

I detta examensarbete undersöks kondensation som en kompletterande tillväxtmekanism för partiklar i den protoplanetära skivan. Denna mekanism bygger på att temperaturen i skivan ökar ju närmare stjärnan man kommer, vilket ger upphov till en så kallad islinje några astronomiska enheter från stjärnan. Innanför islinjen är temperaturen så hög att vatten är i form av ånga, och utanför islinjen så låg att vatten fryser till is. På grund av det låga trycket i skivan kan vatten inte existera i flytande form. Då vattenånga diffunderar utåt i skivan kyls den ner och kondenserar på redan existerande partiklar. En del av dessa ispartiklar rör sig inåt mot stjärnan och förångas återigen, medan de ispartiklar som stannar i den kalla delen av skivan kan växa till betydande storlek genom kondensation.

Resultaten från detta arbete visar att millimeterstora stoftkorn kan växa genom kondensation till ispartiklar med en radie av storleksordningen centimeter till meter. Denna process tar ungefär 1 000 år. Detta är en kort tidsperiod jämfört med den protoplanetära skivans livslängd på några miljoner år, vilket visar att kondensation kan vara en viktig tillväxtmekanism för partiklar i protoplanetära skivor. Partiklarna som bildas är tillräckligt stora för att kunna växa till kilometerstora planetesimaler och därefter planeter genom dynamiska instabiliteter och gravitationell interaktion.



## **Acknowledgements**

Firstly, I would like to thank Anders Johansen, for introducing me to a super-interesting topic and for being a fantastic supervisor; always helpful, encouraging and inspiring.

I would also like to thank Michiel Lambrechts for many, many work-evenings and discussions throughout this project.

Finally, I would like to express my gratitude towards everyone who has helped improving my thesis by asking me questions and giving suggestions. In particular I thank Melvyn B. Davies for very valuable feedback on both a draft and final version of the thesis, and Henrik Hartman for comments on the final version. I thank Kees Dullemond for inviting me to visit the star and planet formation group in Heidelberg to present my work. I would also like to thank Ewine van Dishoeck and Anni Määttänen for helpful suggestions and comments.



# Contents

<b>1</b>	<b>Introduction</b>	<b>11</b>
<b>2</b>	<b>Background</b>	<b>13</b>
2.1	Important observational constraints . . . . .	13
2.2	An overview of different planet formation scenarios . . . . .	14
2.3	Minimum mass solar nebula . . . . .	16
2.4	Dimensionless friction time . . . . .	16
2.5	Turbulence . . . . .	19
2.6	Vertical structure of the disc . . . . .	19
<b>3</b>	<b>Classical coagulation scenario</b>	<b>23</b>
3.1	Overview . . . . .	23
3.2	Bouncing and fragmentation . . . . .	23
3.3	Radial drift . . . . .	25
<b>4</b>	<b>Condensation and clumping scenario</b>	<b>27</b>
4.1	Overview . . . . .	27
4.2	The ice line . . . . .	27
4.3	Condensation and sublimation . . . . .	29
4.4	Streaming instability . . . . .	31
<b>5</b>	<b>Model</b>	<b>33</b>
5.1	Simulation box, units and boundary conditions . . . . .	33
5.2	Superparticle approach . . . . .	34
5.3	Random walk of particles . . . . .	35
5.4	Condensation in a Monte Carlo scheme . . . . .	38
5.5	Test problems . . . . .	40
5.5.1	Test of the dynamical behaviour of the particles . . . . .	40
5.5.2	Test of the condensation algorithm . . . . .	41
<b>6</b>	<b>Results</b>	<b>47</b>
6.1	Overview . . . . .	47
6.2	Atmospheric ice line . . . . .	48
6.2.1	Varying the atmospheric ice line position . . . . .	50
6.2.2	Varying the turbulent $\alpha$ -value . . . . .	52
6.3	Radial and atmospheric ice lines . . . . .	53
6.3.1	Varying the atmospheric ice line position . . . . .	55

## CONTENTS

---

6.3.2	Varying the simulation box size . . . . .	56
6.4	Simulations including a pressure variation . . . . .	57
6.4.1	Varying the atmospheric ice line position . . . . .	59
6.4.2	Varying the simulation box size . . . . .	60
<b>7</b>	<b>Discussion</b>	<b>63</b>
7.1	General assumptions and simplifications . . . . .	63
7.2	Particle structure . . . . .	63
7.3	Particle collisions . . . . .	65
7.4	Connection to observations . . . . .	67
<b>8</b>	<b>Conclusions</b>	<b>69</b>
<b>A</b>	<b>From random walk to the diffusion coefficient</b>	<b>71</b>

# Chapter 1

## Introduction

Planets form in protoplanetary discs of gas and dust, surrounding young stars. In the classical planet formation scenario dust grains collide, stick together and form larger and larger bodies (Safronov 1969). Particles of up to centimeter-sizes stick together due to contact forces and kilometer-sized and larger bodies are held together by gravity. How particles grow from centimeter to kilometer-sized planetesimals is yet not understood, as these particles tend to fragment or bounce off each other as they collide, instead of sticking. Further, meter-sized particles drift rapidly in towards the star, and are therefore lost as possible planet formation material (Brauer et al. 2008).

Sticking, or coagulation, as a growth mechanism has been fairly well studied. However, an often overlooked concept in planet formation models is that of ice lines and growth via condensation.

In this work growth of small ( $\sim 1$  mm) water ice particles via ice condensation is studied computationally. As ice particles drift inwards, they encounter the water ice line where ice sublimates and becomes water vapour. Due to the turbulent motion of the gas in the protoplanetary disc some of the water vapour diffuses back across the ice line into the condensation region where they can condense on to existing ice particles. Many ice particles will move inwards across the ice line and sublimate. However, since small particles are coupled to the gas and thereby move in a random walk due to the turbulence, some of them will also be lucky and stay within the condensation region of the disc, growing significantly as diffusing water vapour condenses on to them.

The water ice line, or condensation front, is found at  $r \approx 3$  AU. As water ice has been estimated to have constituted almost 1% of the total mass in the protosolar nebula, condensation of water is especially interesting for planet formation (Lodders 2003). However, growth by condensation is not only applicable to water ice, but also to any other volatile found in the protoplanetary disc. Other important condensation fronts relevant for planet formation include those of ammonia, methane, carbon monoxide and molecular nitrogen at much larger radii than the water ice line, and that of silicates at  $r \ll 1$  AU (Lodders 2003).

The thesis is structured as follows. After this brief introduction to planet formation and the problem of dust growth, a background chapter follows where some important concepts

---

are introduced. Thereafter, the classical coagulation scenario and its limitations are discussed. An overview of the condensation and clumping scenario, which is in this work proposed as an alternative to or complement to coagulation, is introduced in Chapter 4. The model developed as part of this project is described in Chapter 5, followed by the results in Chapter 6. The limitations of the model and the results are thereafter discussed in Chapter 7, and the conclusions are presented in the final chapter.

## Chapter 2

# Background

### 2.1 Important observational constraints

It is known that planets form in so-called protoplanetary discs, discs of gas and dust around young stars. These discs form together with the star, as the star form by collapse of a molecular cloud (Shu et al. 1987). An overview of star and planet formation is shown in Fig. 2.1.

Today, we can observe these discs and even in some cases directly image them. In the case of the disc around the star LkCa 15 images it is even possible to detect a forming planet within a protoplanetary disc (Kraus & Ireland 2012). From observations we know that the size of these discs are of the order of  $r_{\text{disc}} \approx 100 \text{ AU}$  and  $10^{-4}M_{\odot} < M_{\text{disc}} < 10^{-1}M_{\odot}$  (Beckwith et al. 1990). Observations of protoplanetary discs give important constraints on possible planet formation mechanisms, of which the most important might be the lifetime of the discs. The disc lifetime is the time during which there is still gas left in the disc, with the most important processes removing the gas being accretion onto the central star and photoevaporation of the gas (Alexander et al. 2006). The lifetime of protoplanetary discs has been found to be  $1 - 10 \text{ Myr}$  (Haisch et al. 2001), meaning that any planets need to be formed within this time. This constraint is firm for gas giant planets, as a large fraction of their mass is gas. Terrestrial planets could in principle form without the gas disc being present, as they do not contain significant amount of gas. Focus is therefore in this work on the formation of gas giants, as this is a more difficult task due to the stronger formation time scale constraint.

Unfortunately, most of planet formation is hidden from us due to observational limitations. Thermal emission from dust in the discs has been detected around a significant fraction of young stars (Andrews & Williams 2005), and the growth of these dust grains can be followed up to centimeter-sized grains (Wilner et al. 2005). Bodies of sizes between centimeter-sized grains and planet-sized bodies are however not yet possible to detect directly. This means that from an observational viewpoint we do not have any direct evidence of the possible existence of these.

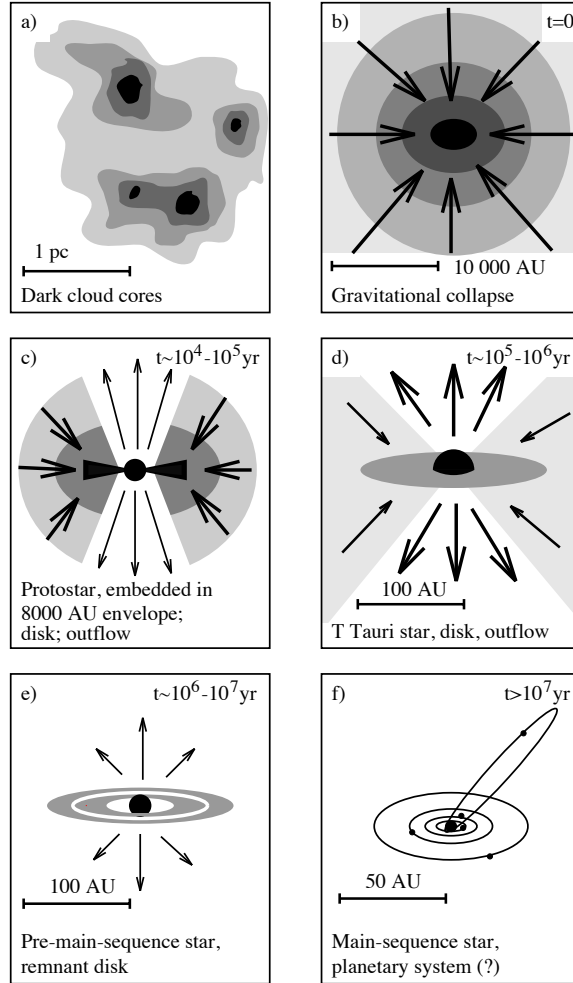


Figure 2.1: Sketch over the different stages of star and planet formation, with relevant time and length scales indicated. a) shows dark cloud cores, which, in b), collapses gravitationally to form a protostar, c), embedded in a gas and dust envelope. d) shows the protoplanetary disc surrounding a young star. This is the relevant stage for this work, as this is where most of the planet formation process takes place. The gas disc dissipates in e) and a planetary system is formed in f). Figure from Hogerheijde (1998).

## 2.2 An overview of different planet formation scenarios

There are two main ideas on how planets can form in the protoplanetary disc. One idea is the gravitational instability hypothesis, in which planets form by gravitational collapse of the gas, similar to how star formation takes place (Boss 2003). This mechanism requires a larger disc mass than observed for most protoplanetary discs, about 10 times more mass than is believed to have been present in the protosolar nebula. Thus, even if this mechanism is operational in a few massive systems, it can not be the main planet forming mechanism. The gravitational instability hypothesis will therefore not be discussed further in this work. Instead, focus

## 2.2. AN OVERVIEW OF DIFFERENT PLANET FORMATION SCENARIOS

---

is on formation of planets in a bottom-up scenario, where small particles collide and stick together, forming larger and larger bodies, and eventually planets (Safronov 1969). The process can be divided into three steps: dust to planetesimals, planetesimals to protoplanets and protoplanets to planets. Table 2.1 shows the sizes of bodies for the three steps, and also the notation used in this work for different sized bodies in the first step.

Step	Notation	Approximate size
1) Dust to planetesimals	Dust	<mm
	Pebbles	cm
	Rocks	dm
	Boulders	m
	Planetesimals	km
2) Planetesimals to protoplanets	Protoplanets	1 000 km
3) Protoplanets to planets	Planets	> 1 000 km

Table 2.1: Planet formation, following the bottom-up scenario, in three steps. The table shows the notation used in this work and approximate size of bodies in the different steps.

This work only addresses growth in the first step, from dust to planetesimals, and more specifically growth from dust to pebbles and rocks. There are different hypotheses describing also this first step from dust to planetesimals. In this work these hypotheses are divided into two broad scenarios: the classical *coagulation scenario* and our proposed *condensation and clumping scenario*.

In the coagulation scenario dust particles collide and stick together, building up larger and larger bodies until planetesimal sizes are reached. This scenario has been thoroughly investigated both numerically (see e.g. Brauer et al. (2008)) and experimentally (see e.g. Blum & Wurm (2008) for a review), but it still remains to be shown that particles can grow all the way from dust to planetesimals via this mechanism. The coagulation scenario is further discussed in Chapter 3.

In this work we investigate an alternative scenario, that of condensation and clumping. In this scenario the condensation of vapour of volatile species onto already existing dust or ice grains aids the growth from dust to pebbles or rocks. As growth via condensation happens at the ice line, where the temperature and pressure conditions are such that a phase change takes place, it naturally enhances the solid material density locally. This opens up for dynamical instabilities, which clump the material further into over-densities that gravitationally can collapse into planetesimals. The condensation and clumping scenario is further discussed generally in Chapter 4, and in the remainder of this work we explore the condensation mechanism as a crucial step in this scenario.

## 2.3 Minimum mass solar nebula

As an underlying model the minimum mass solar nebula (MMSN) model is used to calculate the temperature and density profile of the disc (Hayashi 1981). This model is a theoretical construct, based on the calculated minimum mass needed to form the Solar System. To the observed mass of heavy elements in the planets, hydrogen and helium is added up to a solar concentration. The Solar System is divided into annuli, centered on the current semi-major axis of each planet and extending halfway to the orbit of the neighbouring planets. The augmented mass of each planet is then spread out smoothly over its annulus. This gives the column density  $\Sigma$ , temperature  $T$  and sound speed  $c_s$  as a function of the distance to the star  $r$  (in astronomical units AU) as

$$\Sigma = 1700 r^{-2/3} \text{ g cm}^{-3}, \quad (2.1)$$

$$T = \frac{280}{\sqrt{r/\text{AU}}} \text{ K}, \quad (2.2)$$

$$c_s = 9.9 \times 10^4 \left( \frac{2.34}{\mu} \frac{T}{280} \right) \text{ cm s}^{-1}, \quad (2.3)$$

where  $\mu = 2.34$  is the mean molecular weight of molecular hydrogen. Introducing the Keplerian frequency,

$$\Omega = \sqrt{\frac{GM}{R^3}}, \quad (2.4)$$

where  $G$  is the gravitational constant and  $M$  is the mass of the star, the gas scale height  $H$  of the disc can be written as

$$H = \frac{c_s}{\Omega}. \quad (2.5)$$

These equations form the basis for the model of a protoplanetary disc used in this work.

## 2.4 Dimensionless friction time

Throughout this work, dimensionless friction time,  $\Omega\tau_f$ , is used to denote particle size. In this section this concept is introduced, together with a note on how to translate dimensionless friction time into radius in terms of meters.

In a disc with both gas and solid dust particles moving relative to each other, solids and gas couple through a drag force  $F_d$ . This drag force can be characterized by the friction time  $\tau_f$  (sometimes also called the stopping time  $\tau_s$ ), the time-scale over which a solid particle decreases its velocity with a factor of  $e$  with respect to the gas. A small  $\tau_f$  thus corresponds to a strong coupling between solid and gas, where the smallest particles completely follow the gas motions, whereas a large  $\tau_f$  corresponds to a weak coupling.

The exact form of  $\tau_f$  is set by the relevant drag regime, which in turn depends on the relation between the particle radius,  $a$ , and the mean free path of the gas,  $\lambda$ . Different drag regimes and the influence on particle dynamics has been explored by e.g. Weidenschilling (1977). In

## 2.4. DIMENSIONLESS FRICTION TIME

---

words, a particle with  $a \lesssim \lambda$  can be seen as interacting with the gas through individual collisions with the gas molecules, whereas a particle with a larger radius compared to the mean free path of the gas can be seen as moving through a fluid. The former case corresponds to Epstein drag regime, and the latter to Stokes drag regime. The precise transition between the regimes is  $a = (9/4)\lambda$ , giving the two relevant drag regimes as

$$\begin{aligned} a < (9/4)\lambda & \quad \text{Epstein drag,} \\ a \geq (9/4)\lambda & \quad \text{Stokes drag.} \end{aligned} \quad (2.6)$$

Thus, as particles grow past this size relative to the mean free path of the gas, the drag regime changes from Epstein to Stokes. To take this into account, first the particle size at which this happens will be determined. Then, since the particle size throughout this work is in units of dimensionless Epstein friction time, a scaling from Stokes to Epstein friction time will be determined. Throughout this work, whenever friction time is used without specifying drag regime, this should be interpreted as Epstein friction time.

Eq. 2.6 gives the transition between Epstein and Stokes drag regime in terms of particle radius. As the particle size throughout this work is expressed in terms of dimensionless (Epstein) friction time, the first step is to express this transition in terms of dimensionless friction time instead of radius. Friction time in Epstein drag regime is linear with radius and can be written as

$$\tau_f = \frac{a\rho_\bullet}{c_s\rho_g}, \quad (2.7)$$

where  $a$  is particle radius,  $\rho_\bullet$  material density,  $c_s$  sound speed and  $\rho_g$  gas density. Multiplying both sides with the Keplerian orbital frequency  $\Omega$  gives the dimensionless friction time, which can be further simplified, using the expression for scale height  $H = c_s/\Omega$  from Eq. 2.5, to give

$$\Omega\tau_f = \frac{a\rho_\bullet}{H\rho_g}. \quad (2.8)$$

Rearranging Eq. 2.8 gives the particle radius in terms of dimensionless friction time, so that the transition from Epstein to Stokes drag regime in Eq. 2.6 can be expressed in terms of dimensionless friction time instead of radius,

$$\Omega\tau_f > \frac{9}{4} \frac{\lambda\rho_\bullet}{H\rho_g}. \quad (2.9)$$

The mean free path can be written in terms of the number of molecules  $n$  and the molecular cross-section of molecular hydrogen  $\sigma_{\text{mol}}$ , which is the dominant species of the gas,

$$\lambda = \frac{1}{n\sigma_{\text{mol}}}, \quad (2.10)$$

where  $n = \rho_g/\mu$  is the ratio of gas density to mean molecular weight of the gas. The gas density in the midplane of the disc can be written as

$$\rho_g = \frac{\Sigma_g}{\sqrt{2\pi}H}, \quad (2.11)$$

## 2.4. DIMENSIONLESS FRICTION TIME

---

where  $\Sigma_g$  is the column density of the gas (Hayashi 1981). With Eqs. 2.10 and 2.11, Eq. 2.8 can be written as

$$\Omega\tau_f > \frac{9\pi}{2} \frac{\mu H \rho_\bullet}{\sigma_{\text{mol}} \Sigma_g^2}. \quad (2.12)$$

Assuming a distance from the central star of  $r \approx 4 \text{ AU}$ , numerical values for the scale height and gas column density can be found from Eqs. 2.5 and 2.1, with  $\mu = 3.9 \times 10^{-24} \text{ g}$  and  $\sigma_{\text{mol}} = 2 \times 10^{-15} \text{ cm}^2$  (Nakagawa et al. 1986). The material density of ice is  $\rho_\bullet = 1 \text{ g cm}^{-3}$ . This gives the transition radius from Epstein to Stokes drag regime in terms of dimensionless friction time as

$$\Omega\tau_f > 1.7. \quad (2.13)$$

Whenever particles grow to this size, their coupling to the gas is thus described by Stokes friction time instead of Epstein friction time. The next step is therefore to find a scaling between friction times in the two drag regimes.

Friction time in Epstein drag regime as a function of particle radius was shown in Eq. 2.7. In Stokes regime the friction time is no longer linear in radius, but goes as  $\tau_f^{(\text{St})} \sim a^2$ . The full expression is

$$\tau_f^{(\text{St})} = \frac{4}{9} \frac{\rho_\bullet a^2}{\rho_g c_s \lambda}. \quad (2.14)$$

Non-dimensionalizing Eq. 2.14 by multiplying both sides with  $\Omega$  and using

$$H = \frac{c_s}{\Omega}, \quad \lambda = \frac{\mu}{\rho_g \sigma_{\text{mol}}} \quad \text{and} \quad \rho_g = \frac{\Sigma_g}{\sqrt{2\pi} H}, \quad (2.15)$$

gives the dimensionless Stokes friction time as a function of dimensionless Epstein friction time as

$$\Omega\tau_f^{(\text{St})} = \frac{2}{9\pi} \frac{\sigma_{\text{mol}} \Sigma_g^2}{\mu \rho_\bullet H} (\Omega\tau_f)^2, \quad (2.16)$$

or, using the same numerical values as for Eq. 2.12,

$$\Omega\tau_f^{(\text{St})} \approx 0.6 (\Omega\tau_f)^2. \quad (2.17)$$

This conversion factor is used whenever the particles are larger than the transition size between Epstein and Stokes regime, given by Eq. 2.13, in order to mimic the coupling to the gas correctly.

For easier interpretation, dimensionless Epstein friction time is in this work always used in figures and for results. It is only while actually calculating the particle dynamics in the code that the conversion factor between Epstein and Stokes regime is used. To understand figures and results in terms of radius in meters one can therefore rearrange Eq. 2.8, to obtain  $a$  as a function of  $\Omega\tau_f$  as

$$a = \frac{\Omega\tau_f H \rho_g}{\rho_\bullet}. \quad (2.18)$$

Using  $\rho_\bullet = 1 \text{ g cm}^{-3}$  and calculating  $H(r = 3 \text{ AU})$  and  $\rho_g(r = 3 \text{ AU})$  from MMSN one finds that the dimensionless friction time corresponds approximately to particle radius in meters.

## 2.5 Turbulence

In a protoplanetary disc solids are mixed due to turbulence. Introducing the dimensionless parameter  $\alpha$ , the turbulence in an accretion disc can be written as

$$D = \alpha c_s H. \quad (2.19)$$

as first introduced by Shakura & Sunyaev (1973) in the context of black hole accretion discs, but equally usable for other accretion discs, such as protoplanetary discs. Here  $\alpha$  is thus a non-dimensional parameter that determines the amount of turbulence in the disc. Observations suggests an  $\alpha$ -value in the range between  $10^{-4}$  and  $10^{-2}$ , with a preference towards  $10^{-2}$  (Hartmann et al. 1998).

Computer simulations by Johansen & Klahr (2005) have shown that turbulent transport of small particles in a protoplanetary disc is well described by diffusion. This was done by comparing the dust density from a modelled sedimentation-diffusion equilibrium with the analytical solution. The results showed that turbulent transport of particles of  $\Omega\tau_f \approx 10^{-7}$  (or  $0.1 \mu\text{m}$ -sized pebbles at  $r = 5 \text{ AU}$ ), is described very well by diffusion, but also for larger particles the diffusion-description is fairly accurate (Johansen & Klahr 2005).

## 2.6 Vertical structure of the disc

The vertical structure of the disc is dominated by hydrostatic equilibrium between gravity and pressure gradient. Consider a fluid element at height  $z$  above the midplane and at a distance  $d$  from the central star. The distance from the fluid element to the central star projected on the midplane is  $r$ . The gravity from the central star acting on the fluid element,

$$g = \frac{GM_*}{d^2}, \quad (2.20)$$

can be decomposed in a vertical component  $g_z$  and a radial component  $g_r$ .

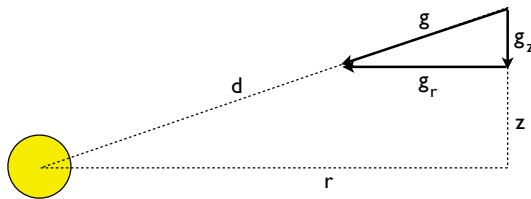


Figure 2.2: Sketch of distance and gravity triangle.

Since the distance triangle ( $d - r - z$ ) and the gravity triangle ( $g - g_r - g_z$ ) are similar triangles we can write  $g_z/g = z/d$ , leading to

$$g_z = g \frac{z}{d} = -\frac{GM_*}{d^2} \frac{z}{d}, \quad (2.21)$$

## 2.6. VERTICAL STRUCTURE OF THE DISC

---

and assuming the disc is thin we can write

$$g_z \approx -\frac{GM_*}{r^3}z = -\Omega^2 z, \quad (2.22)$$

where  $\Omega$  is the Keplerian frequency defined in Eq. 2.4. Including also the gas pressure we can write the equation of motion for the fluid element as

$$\frac{dv_z}{dt} = -\Omega^2 z - \frac{1}{\rho} \frac{dP}{dz}. \quad (2.23)$$

Assuming hydrostatic equilibrium,

$$0 = -\Omega^2 z - \frac{1}{\rho} \frac{dP}{dz}, \quad (2.24)$$

and using  $P = c_s^2 \rho$ , we get

$$0 = -\Omega^2 z - c_s^2 \frac{d \ln \rho}{dz}.$$

Writing  $c_s = H\Omega_K$  gives

$$\begin{aligned} 0 &= -\Omega^2 z - H^2 \Omega_K \frac{d \ln \rho}{dz} \\ &\Rightarrow \frac{d \ln \rho}{dz} = -\frac{z}{H^2}. \end{aligned} \quad (2.25)$$

Solving this equation gives

$$\ln \rho(z) = \ln \rho_0 - \frac{z^2}{2H^2}, \quad (2.26)$$

$$\text{or} \quad \rho(z) = \rho_0 \exp \left[ -\frac{z^2}{2H^2} \right]. \quad (2.27)$$

$\rho_0 = \rho(z = 0)$  is the midplane density, and the connection between  $\rho_0$  and  $\Sigma$  comes from integrating

$$\Sigma = \int_{-\infty}^{\infty} \rho(z) dz = \rho_0 \int_{-\infty}^{\infty} \exp \left[ \frac{-z^2}{2H^2} \right] dz. \quad (2.28)$$

Using the integration rule  $\int_{-\infty}^{\infty} \exp[-ax^2] dx = \sqrt{\frac{\pi}{a}}$  the gas density in the midplane is obtained as

$$\rho_0 = \frac{\Sigma}{\sqrt{2\pi}H}. \quad (2.29)$$

The flux of particles relative to the midplane can be written

$$\mathcal{F}_z = v_z \rho_p - D \rho_g \frac{\partial(\rho_p/\rho_g)}{\partial z}, \quad (2.30)$$

## 2.6. VERTICAL STRUCTURE OF THE DISC

---

assuming Fickian diffusion, meaning that the diffusive flux is proportional and in opposite direction to the gradient of the concentration. Assuming equilibrium between diffusion and sedimentation,  $\mathcal{F}_z = 0$ , and writing  $\epsilon = \rho_p/\rho_g$  for simplicity, we can write

$$0 = v_z \epsilon - D \frac{\partial \epsilon}{\partial z}. \quad (2.31)$$

Introducing the equation of motion of the particles,

$$\frac{dv_z}{dt} = \Omega^2 z - \frac{1}{\tau_f} v_z, \quad (2.32)$$

gives the terminal velocity of the particles by setting  $dv/dt = 0$ , as

$$v_z = -\Omega^2 \tau_f z. \quad (2.33)$$

Inserting the terminal velocity  $v_z$  in Eq. 2.31 gives

$$-\frac{\Omega^2 \tau_f z}{D} = \frac{1}{\epsilon} \frac{\partial \epsilon}{\partial z}, \quad (2.34)$$

which can be rewritten as

$$\frac{\partial \ln \epsilon}{\partial z} = -\frac{\Omega^2 \tau_f z}{D}. \quad (2.35)$$

By writing the diffusion coefficient as  $D = \alpha H^2 \Omega$  and defining  $H_\epsilon^2 = H^2 \alpha / (\Omega \tau_f)$  we find

$$\frac{\partial \ln \epsilon}{\partial z} = -\frac{z}{H_\epsilon^2}, \quad (2.36)$$

which can be solved to give the dust to gas ratio as a function of  $z$  as

$$\epsilon(z) = \epsilon_0 \exp \left[ \frac{-z^2}{2H_\epsilon^2} \right], \quad (2.37)$$

where  $\epsilon_0$  is the dust-to-gas ratio in the midplane. The scale-height of the dust-to-gas ratio is thus

$$\frac{H_\epsilon^2}{H^2} = \frac{\alpha}{\Omega \tau_f}. \quad (2.38)$$

To find the scale height of the particles  $H_p$  the particle density  $\rho_p = \epsilon \rho_g$  can, using Eq. 2.27 and Eq. 2.37, be written as

$$\begin{aligned} \rho_p(z) &= \epsilon_0 \exp \left[ -\frac{z^2}{2H_\epsilon^2} \right] \rho_0 \exp \left[ -\frac{z^2}{2H^2} \right] \\ &= \rho_{p0} \exp \left[ -\frac{z^2}{2H_p^2} \right], \end{aligned} \quad (2.39)$$

and the scale height of particles,  $H_p$ , can be written on the form

$$\frac{1}{H_p^2} = \frac{1}{H_\epsilon^2} + \frac{1}{H^2}. \quad (2.40)$$

## 2.6. VERTICAL STRUCTURE OF THE DISC

---

Inserting Eq. 2.38 into Eq. 2.40 and rearranging leads to a final expression for the particle to gas scale height ratio as

$$\frac{H_p^2}{H^2} = \frac{\alpha}{\Omega\tau_f + \alpha}. \quad (2.41)$$

This is the resulting particle scale height, found from considering sedimentation and turbulent diffusion as driving the particle dynamics in the vertical direction of the disc.

## Chapter 3

# Classical coagulation scenario

### 3.1 Overview

Being perhaps the most intuitive way to form planets from an initial state of dust grains, coagulation has long time been discussed as a planet formation mechanism (Safronov 1969). However, laboratory experiments on particle collisions and computer simulations of dust growth by coagulation, have shown that it is difficult to reach larger particle sizes than millimeters within the life time of a protoplanetary disc (Blum & Wurm 2008; Brauer et al. 2008; Windmark et al. 2012). Up to millimeter-sized dust grains can stick together via van der Waals-forces when colliding, and kilometer-sized planetesimals can sweep up mass via gravitational forces, but particles of sizes in-between do not grow as easily. This chapter gives a brief overview of the most important factors limiting growth by coagulation, focusing on fragmentation, bouncing and radial drift of particles.

### 3.2 Bouncing and fragmentation

The basic idea of the coagulation scenario is that particles in the disc move relative to each other and therefore have the possibility to collide and stick together. Relative velocities are caused by Brownian motion, differential settling, turbulent diffusion and radial drift towards the central star (Brauer et al. 2008). Brownian motion is the thermal velocities of the particles, important for very small particles, but no longer significant for particles larger than micrometers, compared to other sources of relative velocities. Differential settling is caused by the gravity towards the midplane, making different-sized particles reach different sedimentation velocities. Turbulent diffusion was discussed in Section 2.5, and is most important for up to approximately meter-sized particles, or  $\Omega\tau_f \approx 1$ . Radial drift of particles towards the central star, which will be discussed in Section 3.3, peaks for particles of  $\Omega\tau_f \approx 1$ . The total relative velocities of particles in the inner disc ( $r = 1$  AU), including all four sources of relative velocities mentioned above, was calculated by Brauer et al. (2008) and is shown in Fig. 3.1.

### 3.2. BOUNCING AND FRAGMENTATION

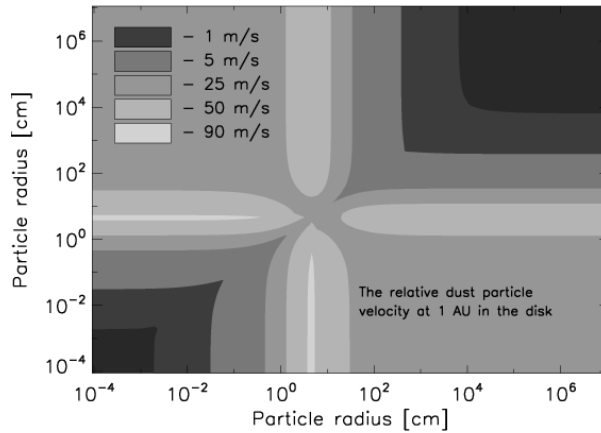


Figure 3.1: Relative velocities of dust particles at 1 AU. Dark colours correspond to low velocities and bright colors to high velocities. Particle sizes are given in centimeters. Figure from Brauer et al. (2008).

The relative velocities between small equal-sized particles are thus low, whereas centimeter- to meter-sized particles collide with velocities of up to  $90 \text{ ms}^{-1}$ . The outcome of collisions between particles of different relative velocities can be tested experimentally (Blum & Wurm 2008), and the results used in computational dust growth models (Brauer et al. 2008; Windmark et al. 2012). The general result is that particle collisions with realistic relative velocities in a protoplanetary disc can lead to sticking for small,  $a \lesssim 1 \text{ mm}$ , particles. This is because small particles collide with low relative velocities, combined with the fact that they are small enough to stick together via van der Waals-forces. Particles that are too large to stick together due to contact forces, also collide with higher relative velocities. In Fig. 3.2, the results from a dust coagulation model by Windmark et al. (2012), incorporating calculated relative velocities in a protoplanetary disc, and results from particle collision experiments, are shown. Particles up to millimeter-sizes can grow via mutual collisions, whereas a possible, although slow, growth mechanism for particles larger than decimeters is that of collisions with many small dust grains. The green regions in the figure shows regions where growth is possible, whereas the yellow and red regions stops coagulation. The yellow region is the bouncing barrier, where particles bounce without neither growing nor decreasing their mass. The upper right corner, marked in red, is the region where collisions lead to fragmentation or erosion. This means that it is extremely difficult to grow particles past these regions, as the only way is by collisions between one large and many very small particles. The results from Windmark et al. (2012) agrees with results from previous dust coagulation models (for example Brauer et al. (2008) in that bouncing and fragmentation of particles effectively stops the growth via coagulation at millimeter-sized particles.

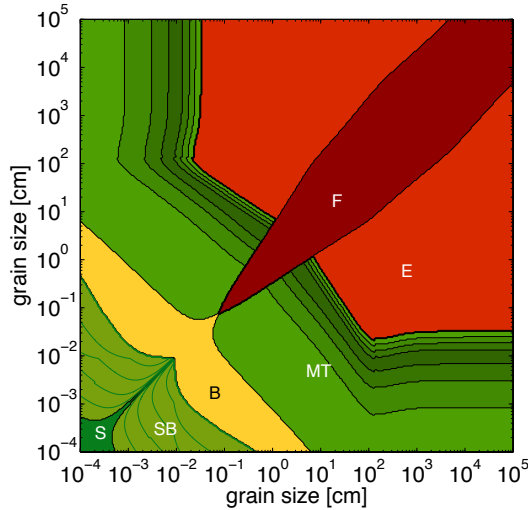


Figure 3.2: Outcome of dust coagulation model incorporating calculated relative particle velocities and results from particle collision experiments. The abbreviations denote collision outcome, with S=Sticking, SB=Sticking or Bouncing, B=Bouncing, MT=Mass Transfer, E=Erosion and F=Fragmentation. In order for a particle to grow larger than millimeters via coagulation it needs to cross the bouncing barrier (yellow). Figure from Windmark et al. (2012)

### 3.3 Radial drift

The protoplanetary disc consists of gas and dust orbiting the star. Particles drift radially inwards because of two different reasons. Firstly, the accretion onto the central star causes particles to drift inwards with the gas. This process is most important for small particles that are tightly coupled to the gas, i.e. for solids with  $\Omega\tau_f \ll 1$ . For particles with  $\Omega\tau_f > 1$  the gas motions become less important and they do not follow the motions of the gas.

The second source of radial drift is the motions of individual particles themselves, due to interaction with the gas in the disc (Weidenschilling 1977). Without gas, the dust would move in Keplerian orbits around the star, with the Keplerian frequency  $\Omega$ . However, since the disc has a higher density and temperature closer to star than further away from it, there is a pressure gradient pointing towards the star. The pressure gradient itself does not affect the dust and larger particles, but it causes the gas to orbit slightly slower than Keplerian. Therefore, the dust feels a headwind from the slower gas, which causes the larger particles to lose angular momentum and drift inwards towards the star.

Figure 3.3, from Brauer et al. (2008), shows the total radial velocity, due to accretion and individual particle drift, as a function of dimensionless friction time (equivalent to Stokes number). The uniform accretion velocity of the gas is represented by the dotted line, and the solid line shows the radial drift of the particles, due to the gas headwind.

### 3.3. RADIAL DRIFT

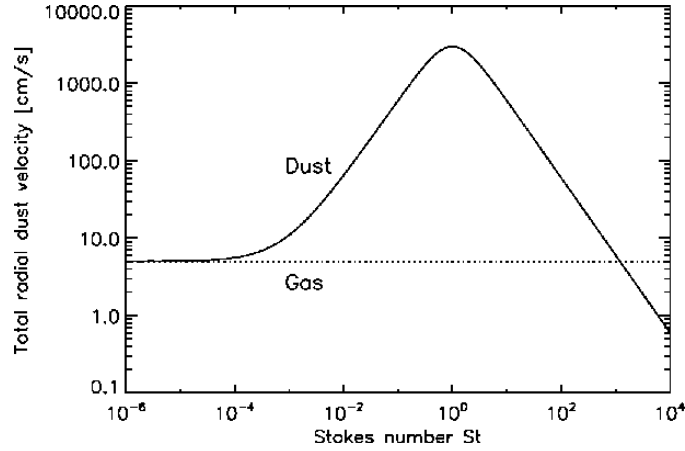


Figure 3.3: Total radial velocity as a function of dimensionless friction time, where  $\Omega\tau_f = St$ . The radial drift peaks for particles with  $\Omega\tau_f \approx 1$ . The plateau to the left corresponds to the gas accretion rate of about  $5 \text{ cm s}^{-1}$ . Figure from Brauer et al. (2008).

From this figure it is clear that the radial drift is fastest for particles of  $\Omega\tau_f \approx 1$ , or meter-sized boulders at 5 AU (Brauer et al. 2008). Starting from 1 AU, these particles drift into the silicate sublimation zone in about 100 years. However, the mechanism is significant also for smaller particles, with only about 5% of the initial mm-sized dust grains and cm-sized pebbles remaining in the disc after  $10^6$  years, as shown by Brauer et al. (2008). Radial drift is thus a problem for planet formation as it leads to a significant loss of solid material. This is not only limiting for the coagulation scenario, but for all scenarios in which particles of meter-sizes are needed in order to reach planetesimal-sizes. However, as is argued in Chapter 4, it is possible to construct planet formation scenarios in which particles move directly from centimeters to kilometers by clumping due to dynamical instabilities.

## Chapter 4

# Condensation and clumping scenario

### 4.1 Overview

The temperature gradient in the protoplanetary disc leads to the existence of ice lines, where a volatile species exist as a solid far from the star, and as vapour closer to the star. Due to the turbulent mixing in the disc, solids drift past the ice line and sublimate. Some of this vapour diffuses back across the ice line and condense out as rims on the already existing solid particles. Although many ice particles sublimate in this process, the ones remaining in the condensation zone experience significant growth. The ice line and the condensation mechanism is discussed in Sections 4.2 and 4.3.

Condensation as a growth mechanism provides a natural way of accumulating solid material, as growth happens close to an ice line. These dense particle regions can collapse directly into planetesimals, by means of dynamical and gravitational instabilities. This step is briefly discussed in Section 4.4.

The word *condensation* is in this work used for the phase transition from vapour to solid, sometimes referred to as deposition in the literature.

### 4.2 The ice line

A protoplanetary disc is heated partly by irradiation from the central star, i.e. direct stellar light absorbed in the surface layers of the disc. This energy is redistributed by the dust grains in the disc by re-emission of the radiation. The other part of the heating is accretional heating. For all but strongly accreting disks, irradiation dominates over accretional heating except for in the midplane, which means that the disc has a colder midplane and hotter surface layers (Dullemond et al. 2007). Water is present in a protoplanetary disc as water vapour and ice, but not in its liquid phase. The temperature structure of the disc means that close to the star water will exist only in vapour form, whereas further out all water will be frozen to ice, with the transition between the two phases called the ice line. In the midplane, the transition is at about 3 AU (see Fig. 4.1). However, since the temperature at a given radius  $r$  increases with the height above the midplane  $z$ , the ice line will not only be a straight vertical line, but a

## 4.2. THE ICE LINE

curved one that also gives a horizontal ice line, as shown in Fig. 4.1. The transition between vapour and ice in the radial direction is referred to as the radial ice line, and the transition between the two phases when changing the height above (or below) the midplane is called the atmospheric ice line.

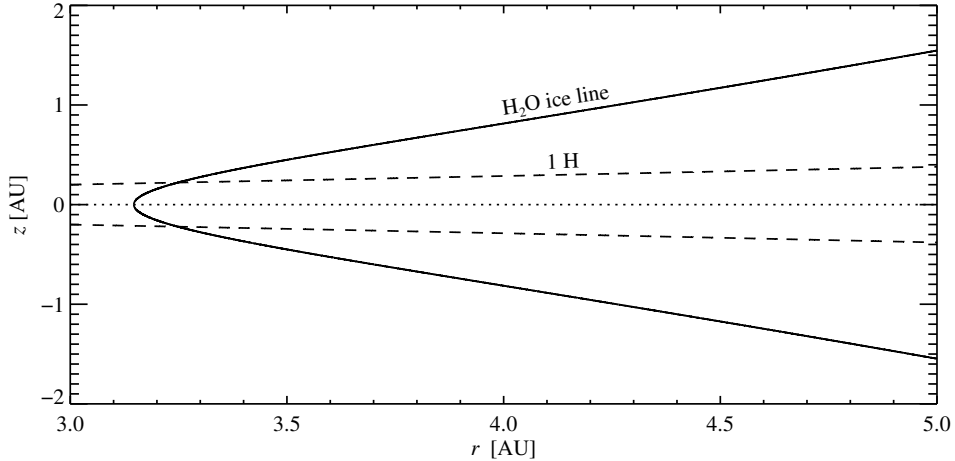


Figure 4.1: Position of the ice line, solid line, at different radii in the protoplanetary disc. The dotted line is the midplane,  $z = 0$  AU, and the dashed line corresponds to one gas scale height  $1 H$ .

In Fig. 4.1, a Minimum Mass Solar Nebula profile is assumed (Hayashi 1981), so that the temperature, sound speed and scale height are given by Eqs. 2.2, 2.3 and 2.5. The pressure exerted by vapour in a system in equilibrium between sublimation (or evaporation, for a liquid-vapour system) and condensation, is called the saturated vapour pressure. It varies with the temperature of the system and has been found experimentally to be

$$P_{\text{sat}} = 6.034 \times 10^{11} \exp(-5938 \text{ K}/T) \text{ N m}^{-2} \quad (4.1)$$

(Haynes et al. 1992). The ice line is here defined to be at the position where the vapour pressure of  $\text{H}_2\text{O}$  is equal to  $P_{\text{sat}}$ . At this point sublimation and condensation are in equilibrium. In the radial direction, sublimation dominates further in towards the star and condensation further out. At distances to the central star greater than the position of the radial ice line, sublimation dominates at large  $|\pm z|$ , whereas in the midplane condensation is the most important process. The water vapour pressure can be found using a hydrostatic gas density profile from Hayashi (1981) of

$$\rho_g = \frac{\Sigma(r)}{\sqrt{2\pi}H(r)} \exp\left(\frac{-z^2}{2H^2}\right), \quad (4.2)$$

$$\text{with} \quad \Sigma = 1700 \text{ g cm}^{-2} \left(\frac{r}{\text{AU}}\right)^{3/2}. \quad (4.3)$$

Assuming a water density of  $\rho = 0.01\rho_g$  (Lodders 2003) and using the ideal gas law

$$P_g = R_s \rho_g T, \quad (4.4)$$

### 4.3. CONDENSATION AND SUBLIMATION

where  $R_s = 461.5 \text{ erg g}^{-1} \text{ K}^{-1}$  is the specific gas constant for water, to rewrite density to pressure, Eq. 4.2 can be written as

$$P_g = 0.01 R_s T \frac{\Sigma}{\sqrt{2\pi} H} \exp\left(\frac{-z^2}{2H^2}\right). \quad (4.5)$$

The ice line is thus positioned at  $r(P_{\text{sat}} = P_g)$ , shown in Fig. 4.1.

Similar “ice lines”, or condensation fronts exist also for other materials at different  $r$ , with e.g. ammonia, methane, carbon monoxide and molecular nitrogen condensing at lower temperatures than water and silicates condensing inwards of 1 AU (Lodders 2003).

### 4.3 Condensation and sublimation

At the ice line ice particles can move into the hotter region and sublimate, and vapour particles can diffuse to colder regions, where they can condense onto existing ice particles. The low pressure in protoplanetary discs makes it impossible for water to exist in liquid form. The pressure-temperature diagram for water is shown in Fig. 4.2

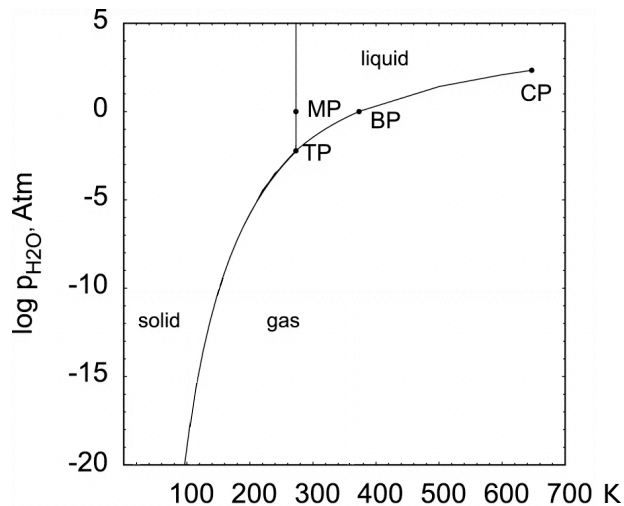


Figure 4.2: Pressure-temperature diagram for water. The curved line shows the saturated vapour pressure, where there is equilibrium between vapour and solid or liquid, and the vertical line marks the equilibrium between liquid and solid. In the low pressures in a protoplanetary disc, water exists only as solid and gas, corresponding to the lower left quadrant of the figure. The pressure is given in units of Atm, where  $1 \text{ Atm} = 1.01325 \times 10^5 \text{ Nm}^{-2}$ , and on the x-axis is temperature in K. TP marks the triple point, where water can coexist in all three phases, MP and BP marks the melting and boiling point for  $P = 1 \text{ Atm}$ , and CP is the critical point where the usual forms of gas and liquid stops existing. Figure adapted from Davis (2007).

To illustrate the physics behind condensation and sublimation we consider a closed system with water in the form of ice and vapour. At all times, there are ice particles sublimating and

### 4.3. CONDENSATION AND SUBLIMATION

---

vapour particles condensing. An equilibrium between the two processes is found when the pressure of the vapour  $P_v$  is equal to the saturated vapour pressure  $P_{\text{sat}}$ . When  $P_v < P_{\text{sat}}$  the vapour is not yet saturated and thus sublimation is the dominating process. For  $P_v > P_{\text{sat}}$  we have saturated vapour and therefore condensation dominates.  $P_{\text{sat}}$  is constant for a given temperature  $T$  and has experimentally (Haynes et al. 1992) been found to be

$$P_{\text{sat}} = 6.034 \times 10^{11} e^{-5938\text{K}/T} \text{ Nm}^{-2}. \quad (4.6)$$

The rate of change in mass for a single ice particle can be written as

$$\frac{dm}{dt} = \text{rate of condensation} - \text{rate of sublimation}, \quad (4.7)$$

where  $m$  is the mass of the ice particle.

Let the ice particle be represented by a sphere with surface area  $4\pi a^2$ , where  $a$  is the radius of the particle. It is surrounded by vapour particles moving with the thermal velocity  $v_{\text{th}}$ . For a vapour particle to be able to hit the ice particle in one time step  $dt$  it must be within a distance  $l \leq v_{\text{th}} dt$  to the ice particle. The volume of vapour particles with a possibility to hit the ice particle in one time step is thus  $dV = 4\pi a^2 v_{\text{th}} dt$ . Assuming all particles within  $dV$  will contribute to the growth of the ice particle  $dm = dV \rho_v$  the expression for the rate of change of the mass of the ice particle, only due to condensation, becomes

$$\frac{dm}{dt} = 4\pi a^2 v_{\text{th}} \rho_v, \quad (4.8)$$

which is valid for perfect condensation. Including also the decrease in mass due to sublimation, the mass change due to condensation and sublimation can be written as

$$\frac{dm}{dt} = 4\pi a^2 v_{\text{th}} \rho_v \left( 1 - \frac{P_{\text{sat}}}{P_v} \right) \quad (4.9)$$

(Supulver & Lin 2000). Rewriting Eq. 4.9 using  $dm = \rho_{\bullet} 4\pi a^2 da$  yields the somewhat simpler expression

$$\frac{da}{dt} = \frac{v_{\text{th}} \rho_v}{\rho_{\bullet}} \left( 1 - \frac{P_{\text{sat}}}{P_v} \right), \quad (4.10)$$

which can be expressed with densities instead of pressures, by considering the ideal gas law

$$P_v = n_v k_B T \quad (4.11)$$

$$= \frac{k_B T}{m_v} \rho_v \quad (4.12)$$

$$= c_s^2 \rho_v, \quad (4.13)$$

where  $n_v$  is the number density of vapour and  $k_B$  is the Boltzmann constant. Equivalently, for the saturated vapour pressure we get

$$P_{\text{sat}} = c_s^2 \rho_{\text{sat}}. \quad (4.14)$$

Eq. 4.10 can now be rewritten as

$$\frac{da}{dt} = \frac{v_{\text{th}}}{\rho_{\bullet}} (\rho_v - \rho_{\text{sat}}). \quad (4.15)$$

#### 4.4. STREAMING INSTABILITY

---

In the limit where  $\rho_v \ll \rho_{\text{sat}}$  sublimation dominates the time evolution, so that the radius change in time can be expressed as

$$\left(\frac{da}{dt}\right)_{\text{subl}} = -\frac{v_{\text{th}}}{\rho_{\bullet}}\rho_{\text{sat}}. \quad (4.16)$$

The time scale for the particle to change its size with a factor of 2,  $\tau_{\text{subl}}$ , can be written as

$$\tau_{\text{subl}} = \frac{a\rho_{\bullet}}{v_{\text{th}}\rho_{\text{sat}}}. \quad (4.17)$$

Correspondingly, as  $\rho_{\text{sat}} \ll \rho_v$  condensation dominates, with time evolution and time scale according to

$$\left(\frac{da}{dt}\right)_{\text{cond}} = \frac{v_{\text{th}}}{\rho_{\bullet}}\rho_v, \quad (4.18)$$

$$\tau_{\text{cond}} = \frac{a\rho_{\bullet}}{v_{\text{th}}\rho_v}. \quad (4.19)$$

From the time evolution equations it can be seen that in the conditions of a protoplanetary disc, with low pressure,  $\tau_{\text{cond}} \gg \tau_{\text{subl}}$ . Further, the change in radius with time due to condensation,  $\dot{a}_{\text{cond}}$ , is independent of the initial radius  $a$ .

#### 4.4 Streaming instability

There are two different types of instabilities that can potentially concentrate particles into clumps. Shear instabilities (e.g. Kelvin-Helmholtz and magnetorotational instabilities) feed on spatial variations in the gas velocity, whereas the streaming instability feeds on velocity differences between gas and particles. A particle clump moving through the gas accelerates the gas around it towards the Keplerian velocity, thereby locally reducing the headwind. The particle clump therefore moves with a speed closer to the Keplerian speed than an isolated particle, resulting in a reduced radial drift for the clump. Since isolated particles have a faster radial drift, they catch up with the clump, resulting in what can be compared to a local growing traffic jam. Computer simulations by Johansen & Youdin (2007) show that the clumping behaviour is strongest for marginally coupled solids, i.e. solids with a dimensionless friction time  $\Omega\tau_f \approx 1$ , corresponding to meter-sized boulders at  $r = 5$  AU. Those clumps had a reduced radial drift velocity of up to 40%. The solids with  $\Omega\tau_f \approx 0.1$ , or rocks of 10 cm at  $r = 5$  AU, formed clumps of smaller scale and shorter life-time. Those clumps had a faster radial drift than lonely particles of the same size as the ones in the clump. This can be explained by the fact that the clump is dense enough for it to be "seen" effectively as one body from the viewpoint of the gas, instead of a clump made up of many small particles.

In later simulations by Johansen et al. (2009b), of solids with  $\Omega\tau_f \approx 0.1$ , the metallicity of the disc was found to influence the clumping behaviour, with a metallicity twice that of the solar value leading to a strong clumping. The simulations showed that the clumps get dense enough to contract and form gravitationally bound clumps with mass equivalent to that of 100-200 km-sized planetesimals (Johansen et al. 2009b).



# Chapter 5

## Model

### 5.1 Simulation box, units and boundary conditions

We simulate a two-dimensional region close to the water ice line at around 3 AU. The simulation domain is set in the radial  $r$  and vertical  $z$  direction, whereas the azimuthal direction is ignored, for simplicity. The fundamental units used are scale heights  $H$  as a length unit, sound speed  $c_s$  as a velocity unit and inverse Keplerian orbits  $\Omega^{-1}$  as a time unit. The relation between these quantities is  $H = c_s/\Omega$  from Eq. 2.5. Setting  $H = c_s = \Omega = 1$  gives a system which is scalable to any region of the protoplanetary disc.

We start by exploring the atmospheric ice line, not including the radial ice line. This means that the simulation domain is just outside of the radial ice line, with a colder midplane and hotter outer layers. The height of the atmospheric ice line above the midplane  $z_{\text{ice}}$  is varied from  $z_{\text{ice}} = 0.2 H$  to  $z_{\text{ice}} = 2 H$ . The lower limit is the lowest value for which not all ice particles immediately sublimate. A lower value gives a distance between the midplane and the ice line which is comparable to the length a particle moves during one time step (see Eq. 5.3), making it possible for all ice particles to escape from the condensation region before any growth has taken place. Setting  $z_{\text{ice}} > 2 H$  does not cause any significant growth. The simulation domain is  $5 H$  in the vertical  $z$ -direction and  $1.25 H$  in the radial  $r$ -direction. The total number of superparticles is  $N = 1\,000$ , where each superparticle represents a large number of physical particles. The initial particle mass is  $m = 10^{-9}$  kg, and as  $\Omega\tau_f \sim m^{1/3}$  the initial ice particle mass in terms of dimensionless friction time is  $\Omega\tau_f = 10^{-3}$ . Periodic boundary conditions are used in both the radial and vertical direction.

Including both the atmospheric and radial ice lines is done by letting the simulation domain represent a region around the radial ice line. This means that ice particles sublimate both by moving away from the midplane, and by moving closer to the central star. The simulation domain is always  $5 H$  in the vertical direction. In the radial direction the box size is varied from  $1.25 H$  to  $5 H$ , with the number of particles and resolution changed accordingly in order to keep the particle density and the effective resolution fixed. Periodic boundary conditions are used in the vertical direction, and reflective boundary conditions in the radial direction. In the vertical direction there is in effect no difference between  $+z$  and  $-z$ , as the conditions above the midplane mirrors those below it. In the radial direction, when including the radial ice line, there is no such symmetry. At  $r = r_{\text{min}}$  conditions such that ice sublimates prevail

at all  $z$ , whereas at  $r = r_{\max}$  the midplane is part of the condensation zone, where ice particles can exist without sublimating. Using periodic boundary conditions in the radial direction would therefore artificially introduce vapour in the system, causing a too large particle growth.

Condensation is considered as a neighbour interaction. A linear scaling between number of particles and number of calculations is obtained by use of a mapping scheme, where the simulation domain is divided into a number of grid cells, with particle interactions possible with particles within the same grid cell only. The default resolution used is  $(n_r, n_z) = (64, 256)$ , where  $n_r$  is the number of grid cells in the radial direction and  $n_z$  the corresponding number for the vertical direction.

## 5.2 Superparticle approach

A superparticle is a numerical representation of a large number of physical particles with the same properties. Here the most important properties are the physical state (ice or vapour), size of constituent particles if ice, and material density. The number of superparticles  $N$  is much smaller than the number of physical particles, so that superparticle  $i$  represents  $n_i$  physical particles. In these simulations, typically  $N = 1\,000$  for a simulation area of  $5 H$  in the vertical direction and  $1.25 H$  in the radial direction, a number chosen to be computationally easy to handle. The number of superparticles is fixed throughout a simulation, and each superparticle represents an equal and fixed mass  $M$  that does not change. The mass  $m$  of the physical particles represented by the superparticle does however change, and so does  $n_i$ , the number of physical particles represented by a superparticle, as the total mass represented by the superparticle is always  $M = m_i n_i$ . Also when an ice particle undergoes a phase transition and becomes vapour the total mass  $M$  of the superparticle stays constant. The superparticle approach to condensation and sublimation is sketched in Fig. 5.1. The short sublimation time scale motivates modelling of sublimation as an instantaneous process, in which an ice superparticle crossing the ice line turns into vapour immediately. Condensation is modelled as a neighbour interaction in a Monte Carlo scheme, described in Section 5.4.

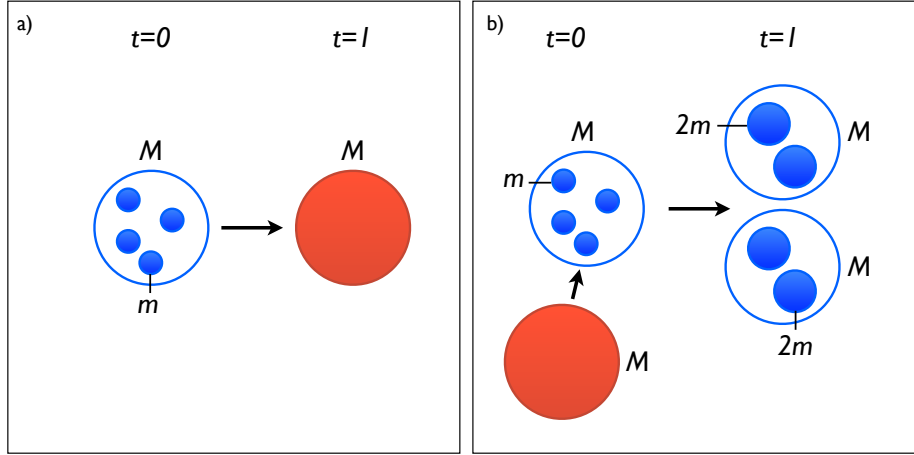


Figure 5.1: Sketch of sublimation and condensation for superparticles. Blue represents ice and red vapour. a) Ice superparticle, representing mass  $M$  in the form of 4 physical ice particles, each of mass  $m$ , sublimates and turns into a vapour superparticle of mass  $M$ . b) Vapour superparticle of mass  $M$  condenses onto an ice superparticle of mass  $M$ , representing the mass  $4m$ . The physical ice particles are after the event represented by two ice superparticles, each representing a total mass  $M$ , but now in the form of 2 physical ice particles each with mass  $2m$ . Both mass and the number of superparticles are conserved between  $t = 0$  and  $t = 1$ . In the case of condensation, also the number of physical particles is conserved.

### 5.3 Random walk of particles

In this section the modelling of particle motions is described. We start by introducing the random walk used to describe the turbulent motions of the gas, sufficient for modelling the motions of small particles, and then move on to include the more complex behaviour of larger particles. As particles grow larger, additional effects need to be taken into account. Firstly, the random step length becomes smaller, as larger particles follow the turbulent eddies a shorter length each time step. Secondly, for larger particles the gravity towards the midplane has an increasingly important effect, causing particles to sediment towards the midplane. Finally, the radial drift towards the central star must be taken into account.

#### Basic model: Random walk

With the dimensionless constant  $\alpha$ , introduced in section 2.5, the turbulence in an accretion disc can be written as

$$D = \alpha c_s H. \quad (5.1)$$

We here assume that particles move with velocity  $v = \sqrt{\alpha} c_s$ , and the length a particle moves per time step is  $l = \sqrt{\alpha} H$ , which gives rise to  $D \sim vl \sim \alpha c_s H$  by mixing length arguments.

### 5.3. RANDOM WALK OF PARTICLES

---

The correlation time is defined as

$$\tau = \frac{l}{v} = \Omega^{-1}. \quad (5.2)$$

In words this means that effect of turbulence on a small particle is to move it in a random direction with a characteristic speed  $v$ , during the correlation time  $\tau$ . The characteristic length-, velocity- and time scales are all set by the turbulence. An  $\alpha$ -value of  $10^{-2}$  is used in the simulations, unless stated otherwise.

The length a particle moves each time step is found by equating the generic expression for the diffusion coefficient,  $D = l^2/4\tau$  (see Eq. A.9), with that of diffusion described by Eq. 5.1, giving

$$l = 2\sqrt{\alpha}H. \quad (5.3)$$

Practically, the random walk for particles coupled to the gas, is modelled by setting the length the particle moves in the radial direction  $\Delta r$  and in the vertical direction  $\Delta z$  to

$$\begin{aligned} (\Delta r)_{\text{rw}} &= l \cos \theta \\ (\Delta z)_{\text{rw}} &= l \sin \theta, \end{aligned} \quad (5.4)$$

where  $0 \leq \theta \leq 2\pi$  is chosen randomly for each particle and time step. This gives a random direction, but a fixed length, for how a particle moves in one time step. This forms the basis of the particle dynamics used in this code, and is valid for small particles perfectly coupled to the turbulent gas. However, for larger particles this simple approximation breaks down. A number of corrections to the random walk model will now be introduced, one at a time, before arriving at the final model for the particle dynamics.

#### Correction 1: Adjusting the random step length

Firstly, the random step length must be adjusted, as larger particles move shorter distance with the turbulent eddies each time step. The diffusion coefficient  $D = vl = l^2\tau = l^2\Omega$  is modified to

$$D^* = \frac{l^2\Omega}{1 + (\Omega\tau_f)^2} = \frac{D}{1 + (\Omega\tau_f)^2} \quad (5.5)$$

following the scheme developed and tested by Youdin & Lithwick (2007). This gives a modified step length, dependent on particle size, of

$$l^* = \frac{2\sqrt{\alpha}H}{\sqrt{1 + (\Omega\tau_f)^2}} = \frac{l}{\sqrt{1 + (\Omega\tau_f)^2}}. \quad (5.6)$$

For small particles  $l^* \approx l$ , whereas for larger particles  $l^* < l$ . Separating the radial and vertical directions, Eqs. 5.4 are replaced by

$$\begin{aligned} (\Delta r)_{\text{rw}} &= \frac{l \cos \theta}{\sqrt{1 + (\Omega\tau_f)^2}} \\ (\Delta z)_{\text{rw}} &= \frac{l \sin \theta}{\sqrt{1 + (\Omega\tau_f)^2}}. \end{aligned} \quad (5.7)$$

**Correction 2: Sedimentation towards the midplane**

As particles grow larger, the gravity towards the midplane influences the particle motion more, leading to a sedimentation towards the midplane of large particles. This affects the vertical direction only, so it is only necessary to modify  $\Delta z$ . This is done by changing the step size in the vertical direction to  $(\Delta z)_{\text{tot}} = (\Delta z)_{\text{rw}} + (\Delta z)_{\text{sed}}$ , where  $(\Delta z)_{\text{sed}}$  is an increasing function of particle size. The sedimentation step length is set by the terminal velocity of the particles  $v_t = -\tau_f \Omega^2 z$  (see Eq. 2.33). However, in order to modify the step length correctly, we must ensure that the resulting particle scale height is the same as the analytically expected scale height. The analytically expected particle scale height resulting from diffusion and sedimentation, given in Eq. 2.41, is

$$\frac{H_p}{H} = \sqrt{\frac{\alpha}{\Omega\tau_f + \alpha}}. \quad (5.8)$$

This is to be compared with the particle scale height from considering a random walk and terminal velocity sedimentation, which is what is used for modelling. The sedimentation time scale is

$$\tau_{\text{sed}} = \frac{z}{|v_t|} \Rightarrow \Omega\tau_{\text{sed}} = \frac{1}{\Omega\tau_f}, \quad (5.9)$$

and the diffusion time scale from a random walk is

$$\tau_d = \frac{H_p^2}{D} \Rightarrow \Omega\tau_d = \frac{H_p^2}{\alpha H^2}, \quad (5.10)$$

leading to a particle scale height of

$$\frac{H_p}{H} = \sqrt{\frac{\alpha}{\Omega\tau_f}}. \quad (5.11)$$

To construct a model that gives the correct scale height, as given by Eq. 5.8, we therefore need to modify the dimensionless friction time to

$$(\Omega\tau_f)^* = \Omega\tau_f + \alpha. \quad (5.12)$$

Changing  $\Omega\tau_f \Rightarrow (\Omega\tau_f)^*$  in Eq. 5.11 reproduces the correct particle scale height given in Eq. 5.8. With the modified dimensionless friction time  $(\Omega\tau_f)^*$  in the terminal velocity expression, the step size in the vertical direction can be written as

$$(\Delta z)_{\text{tot}} = (\Delta z)_{\text{rw}} - (\Omega\tau_f + \alpha)\Omega z \Delta t. \quad (5.13)$$

However, this expression leads to a numerical instability in which large particles overshoot the midplane as they sediment, since for  $\Omega\tau_f > 1$  we get

$$(\Omega\tau_f)^*\Omega z \Delta t > z. \quad (5.14)$$

This gives particle oscillations that are amplified in time. To eliminate this problem, Eq. 5.13 is modified to

$$(\Delta z)_{\text{tot}} = (\Delta z)_{\text{rw}} - \frac{(\Omega\tau_f + \alpha)\Omega z \Delta t}{1 + (\Omega\tau_f)^2}, \quad (5.15)$$

following the scheme of Youdin & Lithwick (2007), which eliminates the amplifying of the vertical particle oscillations. In fact it completely eliminates the oscillations, and instead models its effects by giving the larger particles a long settling time, corresponding to the time they would have spent oscillating before settling. For a comparison between the particle scale height resulting from Eq. 5.15 and the theoretical scale height from Eq. 5.8, see Fig. 5.2. The correlation between the analytical and modelled curve in this figure shows that the particle dynamics in the vertical direction are correctly modelled by Eq. 5.15.

### Correction 3: Radial drift

The step in the radial direction needs to be modified due to the radial drift towards the central star. Also this is particle size dependent, and  $(\Delta r)_{\text{tot}}$  is modified to

$$(\Delta r)_{\text{tot}} = (\Delta r)_{\text{rw}} + (\Delta r)_{\text{rd}} = (\Delta r)_{\text{rw}} - \frac{2\eta v_K}{\Omega\tau_f + (\Omega\tau_f)^{-1}} \Delta t, \quad (5.16)$$

where  $v_K$  is the Keplerian velocity and  $\eta = 0.05 c_s$  is the velocity difference between the gas and the particles, following Weidenschilling (1977). This gives a radial drift velocity that peaks for  $\Omega\tau_f = 1$  particles.

### Final form of equations: Random walk + corrections

The equations used to describe particle dynamics in the code are thus

$$\Delta z = \frac{l \sin \theta}{\sqrt{1 + \Omega^2 \tau_f^2}} - \frac{(\Omega\tau_f + \alpha)\Omega z}{1 + (\Omega\tau_f)^2} \Delta t \quad (5.17)$$

$$\Delta r = \frac{l \cos \theta}{\sqrt{1 + \Omega^2 \tau_f^2}} - \frac{2\eta v_K}{\Omega\tau_f + (\Omega\tau_f)^{-1}} \Delta t, \quad (5.18)$$

where the first term for both the radial and vertical direction describes the random walk, with a step length modified according to particle size, and the second term describes sedimentation and radial drift, for the vertical and radial direction, respectively.

## 5.4 Condensation in a Monte Carlo scheme

Condensation is in effect a neighbour interaction, requiring vapour to be present near an ice particle for interaction to occur. In this model “near” means being in the same grid cell, so that it is possible for an ice particle to interact only with vapour within the same grid cell. Condensation in each time step is thus decided one grid cell at a time. Any grid cell can, and most often does, harbour more than one ice particle. Therefore, if condensation takes place in a given grid cell and a given time step, is decided in a two-step process for each vapour particle present in the grid cell.

The two-step procedure is here described for one grid cell and one time step  $\Delta t$ , with one vapour particle present in this grid cell. In the case where more than one vapour particle is present in the grid cell, the two-step procedure is repeated for each vapour particle present. The first step is to decide whether this vapour particle condenses onto any of the ice particles.

#### 5.4. CONDENSATION IN A MONTE CARLO SCHEME

---

If it does, the second step is to decide which of the ice particles it condenses onto. In this scheme, any vapour particle can only condense onto one single ice particle, it can not be shared amongst more than one ice particle. One ice particle can on the other hand experience several growth events during one time step, if several vapour particles are present.

As a first step it is decided whether or not the vapour particle is involved in a condensation event during the time step  $\Delta t$ . In order to do this the total interaction probability for all ice particles in the grid cell is needed. The interaction probability for ice particle  $i$  is

$$p_i = 1 - \exp(-\Delta t/\tau_i), \quad (5.19)$$

where  $\tau_i$  is the condensation time scale for particle  $i$ , given by

$$\tau_i = \frac{1}{3} \frac{a\rho_{\bullet}}{\rho_v v_{th}}, \quad (5.20)$$

as shown in Chapter 4. The expression for interaction probability is chosen to always give  $0 \leq p_i \leq 1$ , for any  $\Delta t$ , also for  $\Delta t \ll \tau_i$ . For easier calculation, the probability that no interaction occurs is then calculated, rather than just the total interaction probability. For  $n$  ice particles, the total probability that no interaction occurs is calculated as

$$p_0 = (1 - p_1) \cdot (1 - p_2) \cdot \dots \cdot (1 - p_n). \quad (5.21)$$

To decide if condensation occurs, a random number  $r_1 = [0, 1]$  is generated. If  $r_1$  is smaller than  $p_0$  nothing happens, whereas if  $r_1$  is larger than  $p_0$  vapour condenses onto one of the ice particles. If condensation occurs, a second step is needed in order to decide onto which of the ice particles in the grid cell is involved in the interaction. In this step it is no longer the absolute probability that is of interest, but the relative probabilities of the ice particles in the grid cell. This can be expressed as

$$p_i^* = \frac{\Delta t}{\tau_i}. \quad (5.22)$$

The relative probability for each of the ice particles in the grid cell are placed in a sequence,

$$0, p_0^*, p_0^* + p_1^*, p_0^* + p_1^* + p_2^*, \dots, \sum_i p_i^*, \quad (5.23)$$

and a new random number is generated,  $r_2 = [0, \sum_i p_i^*]$ . Which interval in the sequence  $r_2$  falls in decides which ice particle the vapour particle condenses onto, such that  $r_2$  falling in the interval  $[p_{i-1}^*, p_i^*]$  implies condensation onto ice particle  $i$ .

The condensation time scale in Eq. 5.20 is proportional to the radius of the particle, so that smaller particles have a shorter, and larger particles a longer, condensation time scale. This corresponds to a larger condensation probability for smaller particles and vice versa, which may seem counter-intuitive, but is explained by the fact that the simulation handles superparticles, each representing the same mass  $M$ . Therefore a superparticle representing small physical particles represents a larger combined surface area than one that is representing large particles. Condensation is thus more likely to happen to a superparticle representing small particles. Looking at a single-physical-particle-basis, the result is correct averaged over many timesteps and particles. A condensation event means doubling the mass of the physical particles involved, meaning that a small particle experiences many condensation events, but the absolute growth in radius each event is small, whereas a single large physical particle experiences few condensation events, but its absolute radius growth is large in each event.

## 5.5 Test problems

In order to understand the results of the computer simulations and to make sure that the code is functioning correctly, two major tests of the algorithms used were made. Firstly, the dynamical behaviour of the code was tested without including particle growth. Secondly, the particle growth algorithm was tested, without taking the spatial dimensions into account.

### 5.5.1 Test of the dynamical behaviour of the particles

A test of the dynamical behaviour of the particles was made by excluding condensation and sublimation from the simulation. This means that particles move due to turbulence, stirring them up by turbulent diffusion, and gravity towards the midplane, but no particle growth is included. The particles settle to an equilibrium, where the particle scale height depends on the size of the particles, since the strength of the coupling to the turbulent gas is a function of particle size. Fig. 5.2 shows the particle scale height in terms of the gas scale height  $H_p/H$  as a function of particle size, expressed in dimensionless friction time  $\Omega\tau_f$ . The particles are assumed to settle into a Gaussian distribution around the midplane, meaning that the particle scale height in the model can be retrieved as the root mean square of the particle positions,

$$\left(\frac{H_p}{H}\right)_{\text{mod}} = \sqrt{\frac{1}{n} (z_1^2 + z_2^2 + \dots + z_n^2)}, \quad (5.24)$$

where  $n$  is the number of particles and  $z_i$  is the vertical position of a particle. This is compared to the theoretically expected particle scale height, given by an equilibrium between sedimentation and turbulent diffusion,

$$\left(\frac{H_p}{H}\right)_{\text{theo}} = \sqrt{\frac{\alpha}{\Omega\tau_f + \alpha}}. \quad (5.25)$$

For a derivation of the sedimentation-diffusion equilibrium, see Section 2.6.

Fig. 5.2 shows how the particle scale height depends on the size of the particles, with the modelled values represented by the black full line and the expected analytical values as a red dotted line. The modelled line clearly follows the analytical curve, showing that the dynamical behaviour of the particles is as expected. From the figure one can see that small particles are fully coupled to the gas, as  $H_p/H = 1$  for particles of  $\Omega\tau_f \lesssim 10^{-3}$ . This corresponds to  $\sim$  mm-sized ice particles near the water ice line. Further, a slight change of the slope can be seen at  $a \approx 1.7$  m. This change is caused by the change from Epstein to Stokes drag regime, and is explained by the fact that in the Epstein drag regime  $\Omega\tau_f^{(\text{Ep})} \sim a$ , whereas for particles larger than this transition size,  $a \approx 1.7$  m, whereas in the Stokes drag regime, here applicable for particles  $a \gtrsim 1.7$  m, we instead have  $\Omega\tau_f^{(\text{St})} \sim a^2$ .

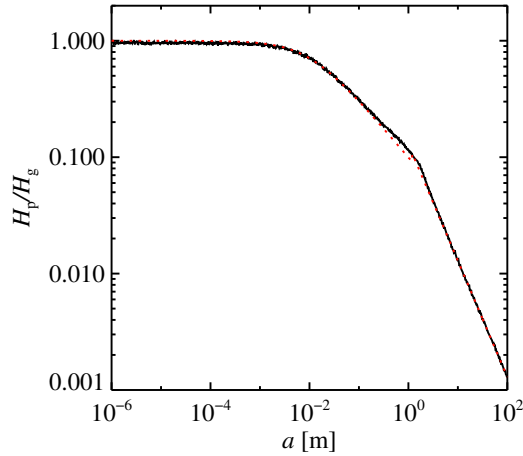


Figure 5.2: Comparison between modelled and analytical particle scale height as a function of particle size. Black full line denotes modelled values and red dotted line analytical values. Small particles  $\Omega\tau_f \lesssim 10^{-3}$  are perfectly coupled to the gas, whereas larger particles sediment towards the midplane. The slope change at  $\Omega\tau_f \approx 1.7$  is due to the change from Epstein to Stokes drag regime. The particle size is given as  $a [\text{m}] \sim \Omega\tau_f^{(\text{Ep})}$ . Overall, modelled and analytical values are in good agreement.

### 5.5.2 Test of the condensation algorithm

The condensation algorithm can be tested by letting particles grow via condensation, without including the spatial dimensions. This means that no ice line is included, and thus sublimation is not taken into account. The number of ice superparticles is known, as is the number of vapour superparticles. The simulation is run until all vapour has condensed onto the ice particles, which means that the total mass available for growth is known. By tracking the initial and final mass of all superparticles the growth in radius is followed, and can be compared to a theoretical expectation. The final radius  $r_{\text{final}}$  is plotted as a function of  $a_{\text{init}}$  as black crosses in Fig. 5.3. Overplotted as red lines are the possible final radii, showed up to 12 condensation events for one ice particle. This clearly shows the discrete behaviour of the Monte Carlo scheme used. In reality, condensation is a continuous process on macroscopic scales, where single water molecules condense onto ice particles so that growth happens little by little all the time. In the Monte Carlo scheme used in this code this continuous behaviour is modelled by a discrete growth process. A condensation event in the code involves one ice superparticle and one vapour superparticle. The mass of the physical ice particles represented by the ice superparticle doubles as the vapour superparticle completely condenses onto the ice. This means that there should be no vapour superparticle left after the event. To conserve the number of particles and superparticles (for easier coding purposes) this implies that the physical ice particles that before the event were represented by the one ice superparticle involved in the event, now are represented by two superparticles, i.e. the number of physical ice particles before the event are after the event split between two ice superparticles. The bottom line of this is that the mass of the physical particles involved in an event doubles

## 5.5. TEST PROBLEMS

as a condensation event occurs. As particle radius is connected to mass as  $m \sim a^3$ , for any number of condensation events  $n_{ce}$  the radius increases as

$$a \rightarrow (2^{n_{ce}})^{1/3} a. \quad (5.26)$$

The expected radius growth from mass doubling events is plotted as red lines in Fig. 5.4, for a different number of condensation events  $0 \leq n_{ce} \leq 12$ . From the figure it is clear that all modelled values indeed fall on these lines, and never in-between. This confirms the expected discrete behaviour of the Monte Carlo method used.

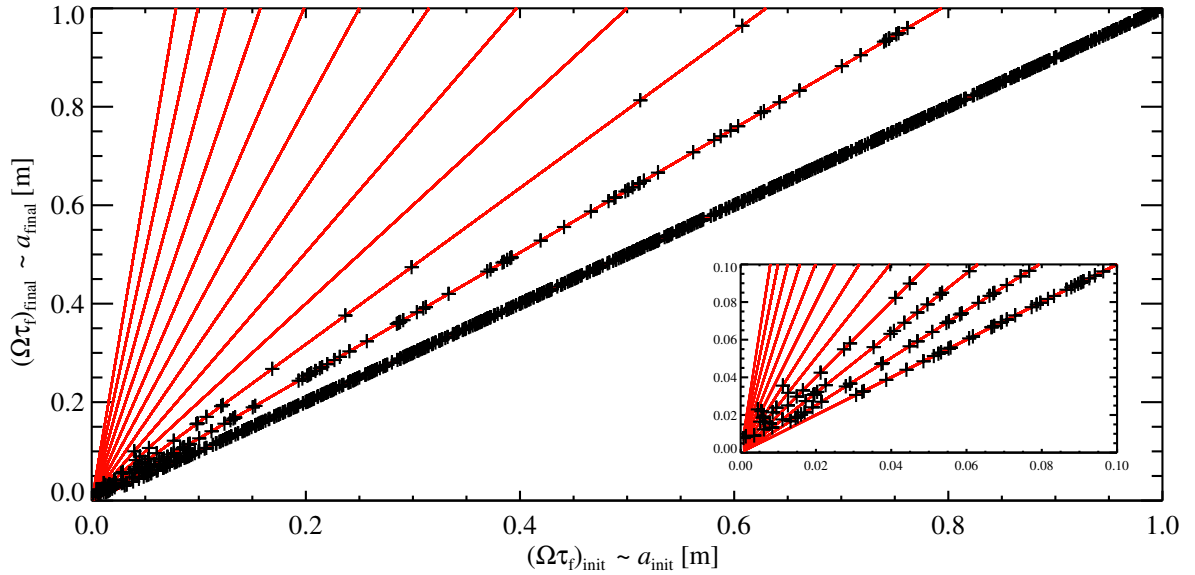


Figure 5.3: Final particle size as a function of initial particle size for an initial number of 1 000 ice superparticles and 10 000 vapour superparticles. Black crosses show modelled values and red lines expected final size for a number of condensation events between 0 (rightmost line) and 12 (leftmost line). Sizes are given as radius in units of dimensionless friction time  $\Omega\tau_f$ . The inlay figure is a zoom in to show the growth for small ( $0 < \Omega\tau_f \leq 0.1$ ) particles, with units being the same as for the main figure.

The modelled particle growth can be compared to the analytically expected  $\Delta a$ . For a physical ice particle  $i$  the total mass growth due to condensation during the time  $\Delta t$  is

$$\Delta m_i = m_i - m_{0,i} = \frac{4\pi}{3} (a_i^3 - a_{0,i}^3) \rho_{\bullet}, \quad (5.27)$$

where  $\rho_{\bullet}$  is the material density of ice,  $a_{0,i}$  is the initial and  $a_i$  the final radius of the ice particle. However, the physical particles are represented by superparticles in the code, and the mass growth must therefore be given for superparticles and not physical particles. One superparticle represents the mass  $M_i = n_i m_i$ , where  $n_i$  is the number of physical particles represented by the superparticles. For one superparticle the mass growth can thus be written as

$$\Delta M_i = M_i - M_{0,i} = \frac{4\pi}{3} (n_i a_i^3 - n_{0,i} a_{0,i}^3) \rho_{\bullet}. \quad (5.28)$$

## 5.5. TEST PROBLEMS

---

The total mass that condenses onto the ice particles during time  $\Delta t$  is given by the difference between the sum of final and initial superparticles,

$$\sum_i \Delta M_i = \frac{4\pi}{3} \rho_{\bullet} \left( \sum_i n_i a_i^3 - \sum_i n_{0,i} a_{0,i}^3 \right). \quad (5.29)$$

The total number of physical ice particles is constant, as is the total number of ice and vapour superparticles, but the number of ice superparticles is not. As the physical particles represented by one superparticle grow in mass, the number of physical particles represented by the superparticle decreases since the total mass of a superparticle is constant. In order to conserve the number of physical particles, total number of superparticles and the total mass of each superparticle, the number of ice superparticles increases as the physical particles grow in mass, so that each superparticle represents fewer and fewer physical particles, which is why the two sums in Eq. 5.29 are over different numbers of superparticles.

The left handside of Eq. 5.29 is simply the total amount of vapour put into the system

$$\sum_i \Delta M_i = M_v = \rho_v V \quad (5.30)$$

and the right handside can be rewritten using

$$n_i = \frac{M_i}{m_i} = \frac{\rho_i V}{\rho_{\bullet} \frac{4\pi}{3} a_i^3}. \quad (5.31)$$

Here  $V$  is the volume represented by a superparticle, which is in this one-grid-cell test problem equal to the total volume of the box. By cancelling terms and gathering the densities on the left handside Eq. 5.29 can be rewritten as

$$\frac{\rho_v}{\rho_i} = N_p - N_{0,p} \quad (5.32)$$

where  $N_p$  and  $N_{0,p}$  is the final and initial number of ice superparticles, respectively. All superparticles represent the same density, and therefore the ratio between the two densities corresponds to the ratio between the number of vapour and ice superparticles represented.  $\rho_v$  is the total vapour density, whereas  $\rho_i$  is the ice density for one superparticle, so that

$$\frac{\rho_v}{\rho_i} = \frac{N_v}{1}, \quad (5.33)$$

with  $N_v$  being the number of vapour superparticles added to the simulation. Eq. 5.29 therefore is equivalent to the very simple expression

$$N_v = N_p - N_{p,0}, \quad (5.34)$$

which the code can be checked against, as both the number of vapour superparticles put into the system, and the initial number of ice superparticles, is specified, and the final number of superparticles is given as an output from the program. This test shows that the code is mass-conserving, as is expected.

From Eq. 5.29 the theoretically expected  $\Delta a$  for each particle can be found. The final radius

## 5.5. TEST PROBLEMS

---

can be rewritten as  $a_i = \Delta a + a_{0,i}$ , where  $a_{0,i}$  is the initial radius of the particle. The two sums are not necessarily over the same number of superparticles, as each condensation event introduces a new ice superparticle in the system, at the expense of the vapour particle representing the condensing vapour. The physical particles originally represented by the first ice superparticle are now split between the new and the old ice superparticle. The initial size of a physical particle represented by a converted vapour superparticle, can therefore be found as the initial size represented by the first ice superparticle. Eq. 5.29 is thereby rewritten as

$$M_v = \frac{4\pi}{3} \rho_{\bullet} \left[ \sum_i n_i (\Delta a + a_{0,i})^3 - \sum_{0,i} n_i a_{0,i}^3 \right], \quad (5.35)$$

which, by using Eq. 5.31, cancelling terms and noting that as in Eq. 5.29  $\rho_v/\rho_i = N_v$ , gives

$$N_v = \sum_i \frac{1}{a_i^3} (\Delta a + a_{0,i})^3 - N_{p,0}. \quad (5.36)$$

The initial number of vapour and ice superparticles  $N_v$  and  $N_{0,p}$  are known, as they are input parameters to the simulation. The radius represented by a superparticle in the end of the simulation,  $a_i$ , and when it is created,  $a_{c,i}$ , are both given as output from the code. The radius growth for each particle  $\Delta a$  can therefore be found by iteration. For  $N_v = 10\,000$  and  $N_{0,p} = 1\,000$ , a value of  $\Delta a \approx 0.0143$  is found. In Fig. 5.4 the red full line represents the expected growth of the 1 000 initial ice superparticles,  $(a_i + \Delta a)$ , as a function of initial radius  $a_{0,i}$ . Comparing the expected final particle radii with the actual final radii shows that for small particle sizes the Monte Carlo method works fairly well, whereas for larger particle sizes most particles experience too little (zero) growth and a few grow several orders of magnitude more than expected. This means that one must be careful not to draw conclusions from the growth of individual particles. However, statistically speaking, i.e. averaging over many particles, the result can be considered to be correct (Zsom & Dullemond 2008). In Fig. 5.4 particles are starting from a non-random initial size distribution, with 20 different initial sizes, and 100 particles of each size. This allows for calculating the mean growth in each initial size bin, shown as blue stars in the figure. Even though there is a spread in growth if considering individual superparticles, this shows that the mean growth in each mass bin roughly follows the expected analytical growth (blue line).

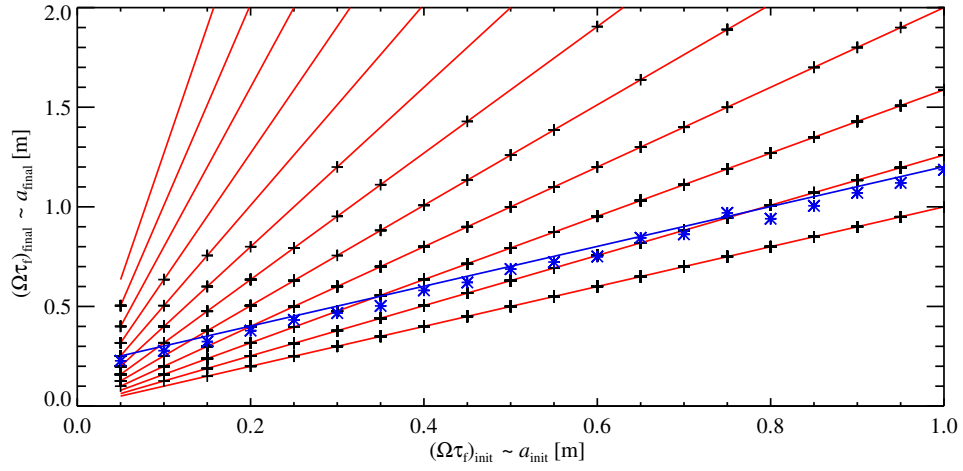


Figure 5.4: Comparison between average modelled growth and analytically expected growth of ice particles. The final particle size as a function of initial particle size is shown for 2 000 ice superparticles in 20 different initial size bins, and with 10 000 vapour superparticles added. Black crosses show modelled values and blue stars show the average growth in each size bin. Note that each black cross can represent more than one ice particle. The modelled average size roughly agrees with the analytical value, shown as a blue line. Red lines denotes expected size for a number of condensation events between 0 (lower line) and 12 (upper line).

## 5.5. TEST PROBLEMS

---

# Chapter 6

## Results

### 6.1 Overview

Simulations including the atmospheric ice line only were performed, as well as simulations including both the atmospheric and the vertical ice line. The parameters for the simulations performed are summarized in Table 6.1.

## 6.2. ATMOSPHERIC ICE LINE

Simulation	$z_{\text{ice}}/H$	$r_{\text{ice}}/H$	$r_{\text{max}}/H$	$\alpha$	PB	Section
1a	0.2	—	0.625	$10^{-2}$	—	6.2.1
1b	0.6	—	0.625	$10^{-2}$	—	6.2.1
1c	1.0	—	0.625	$10^{-2}$	—	6.2.1
1d	1.4	—	0.625	$10^{-2}$	—	6.2.1
1e	1.8	—	0.625	$10^{-2}$	—	6.2.1
2a	$0.2 \leq z_{\text{ice}} \leq 2.0$	—	0.625	$10^{-4}$	—	6.2.2
2b	$0.2 \leq z_{\text{ice}} \leq 2.0$	—	0.625	$10^{-3}$	—	6.2.2
2c	$0.2 \leq z_{\text{ice}} \leq 2.0$	—	0.625	$10^{-2}$	—	6.2.2
3a	0.2	-0.3	0.625	$10^{-2}$	—	6.3.1
3b	0.6	-0.3	0.625	$10^{-2}$	—	6.3.1
3c	1.0	-0.3	0.625	$10^{-2}$	—	6.3.1
3d	1.4	-0.3	0.625	$10^{-2}$	—	6.3.1
3e	1.8	-0.3	0.625	$10^{-2}$	—	6.3.1
4a	1.0	-0.3	0.625	$10^{-2}$	—	6.3.2
4b	1.0	-0.3	1.875	$10^{-2}$	—	6.3.2
4c	1.0	-0.3	3.125	$10^{-2}$	—	6.3.2
4d	1.0	-0.3	4.375	$10^{-2}$	—	6.3.2
5a	0.2	-0.3	0.625	$10^{-2}$	PB	6.4.1
5b	0.6	-0.3	0.625	$10^{-2}$	PB	6.4.1
5c	1.0	-0.3	0.625	$10^{-2}$	PB	6.4.1
5d	1.4	-0.3	0.625	$10^{-2}$	PB	6.4.1
5e	1.8	-0.3	0.625	$10^{-2}$	PB	6.4.1
6a	1.0	-0.3	0.625	$10^{-2}$	PB	6.4.2
6b	1.0	-0.3	1.875	$10^{-2}$	PB	6.4.2
6c	1.0	-0.3	3.125	$10^{-2}$	PB	6.4.2
6d	1.0	-0.3	4.375	$10^{-2}$	PB	6.4.2

Table 6.1: Table of simulations performed. The simulation number is given in the first column. The second column gives the height of the atmospheric ice line above the midplane in terms of scale height,  $z_{\text{ice}}/H$ . The third column indicates whether the radial ice line is included, by giving the position of the radial ice line  $r_{\text{ice}}/H$  where applicable. Column 4 gives the radial extent of the box, as  $r_{\text{max}}/H$ . Column 5 gives the value of the dimensionless turbulent  $\alpha$ -parameter and column 6 indicates whether a pressure bump (PB) was introduced in the simulation. Finally, the last column gives a reference to the section where the results of the simulation can be found.

## 6.2 Atmospheric ice line

As a first step, simulations were run in which the atmospheric ice lines were included, but not the radial ice line. Physically, this is equivalent to a situation where the simulation box is placed slightly outside of the radial ice line. This corresponds to a one dimensional problem, as it is not necessary in this step to take systematic radial motions into account. Thus, radial drift was neglected in these simulations.

## 6.2. ATMOSPHERIC ICE LINE

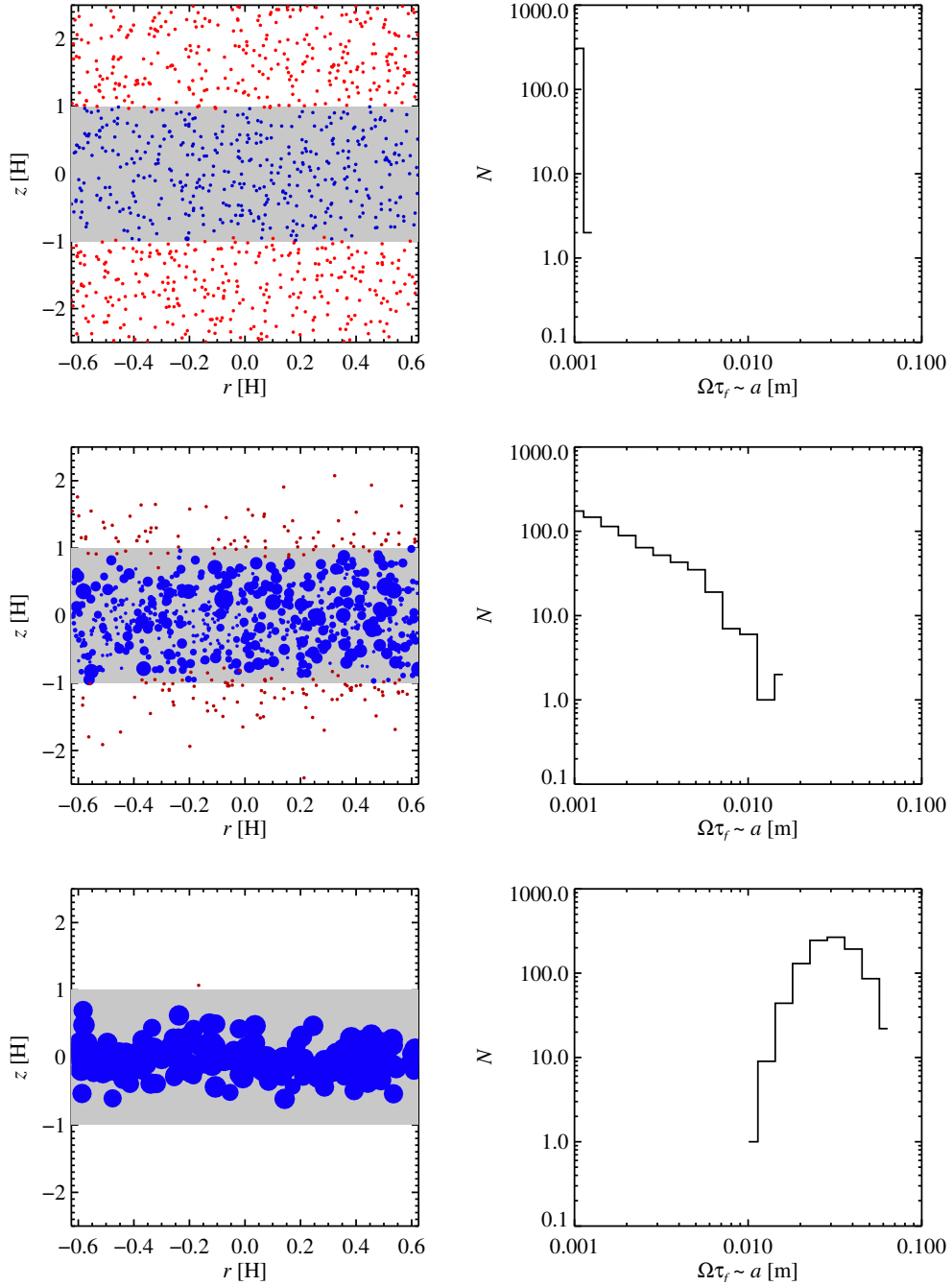


Figure 6.1: Left panels: Distribution of blue ice particles and red vapour particles, for  $t=0$ , 100 and 10 000  $\Omega^{-1}$ , from top to bottom. The grey area corresponds to the condensation zone. The number of particles shown is inversely scaled with size for visibility. Right panels: Size distribution of ice particles, for  $t=0$ , 100 and 10 000  $\Omega^{-1}$ .

Figure 6.1 shows the ice particle growth with time in a typical simulation. To the left the blue dots, representing ice particles, and red dots, representing vapour particles, are shown in the simulation box. The grey area represents the condensation region, corresponding to the

## 6.2. ATMOSPHERIC ICE LINE

---

cold midplane, bordered by the atmospheric upper and lower ice lines. The size of a blue dot is proportional to the logarithm of the physical radius of the ice particle. For visibility, the number of particles shown is inversely scaled with particle radius.

To the right the size distribution of ice particles is shown. The upper row shows the initial state of the system,  $t = 0$ , starting out with  $N = 1\,000$  superparticles, randomly distributed in the simulation domain. The initial position of a particle sets its initial state as being ice or vapour, depending on whether it is inside or outside of the condensation region. From the top right panel it can be seen that the initial number of ice particles is  $N_{\text{ice}} \approx 400$  out of a total of  $N = 1\,000$  ice and vapour particles, corresponding to the fraction of the total simulation area occupied by the condensation zone. In the middle row the system after  $t = 100\,\Omega^{-1}$  is shown, and in the bottom row the system has reached an equilibrium after  $t = 10\,000\,\Omega^{-1}$ . As can be seen, some ice particles grow in time, as vapour particles condense on to them. Meanwhile, smaller ice particles follow the turbulent gas, and have a significant probability to move out from the condensation zone, thus sublimating. This vapour supplies the larger particles with material for growth. As larger particles sediment towards the midplane, they have a smaller probability of reaching the hotter zones and sublimate. This means that when reaching equilibrium the size distribution will have a narrow size distribution, the system consisting almost only of ice particles, large enough to not move out of the condensation zone.

### 6.2.1 Varying the atmospheric ice line position

Simulations were run with the atmospheric ice line placed at different heights  $z_{\text{ice}}$  above the midplane. Decreasing  $z_{\text{ice}}$  corresponds in a physical protoplanetary disc to placing the simulation box radially closer in towards the radial ice line, where a hypothetical  $z_{\text{ice}} = 0$  would correspond to the position of the radial ice line.

## 6.2. ATMOSPHERIC ICE LINE

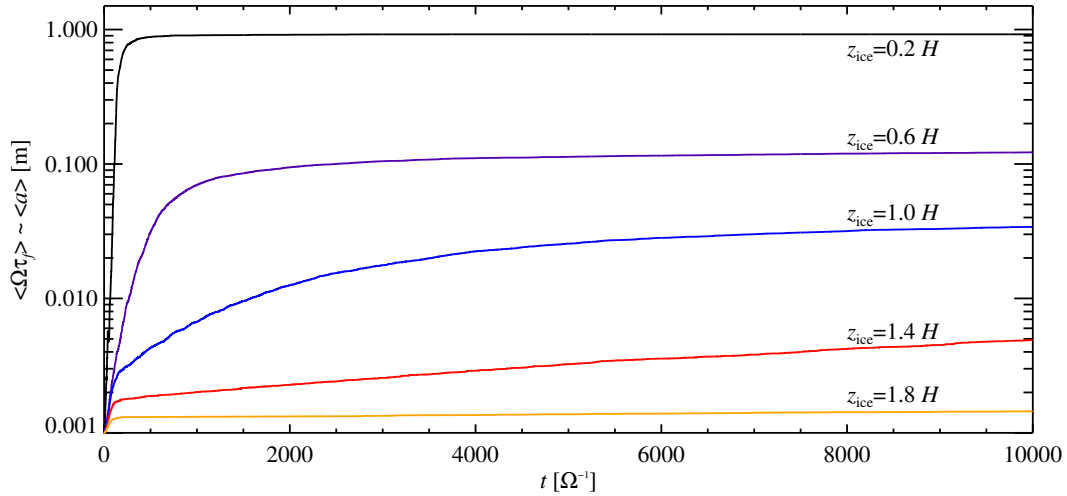


Figure 6.2: Growth dependence on atmospheric ice line position. The mean particle size, expressed in dimensionless friction time  $\langle \Omega \tau_f \rangle$ , is shown as a function of time  $t$  in orbital frequency  $\Omega^{-1}$ , when the system has settled into an equilibrium, after  $t = 10\,000 \Omega^{-1}$ . The different lines show the growth for different distances from the atmospheric ice line  $z_{\text{ice}}$  to the midplane. From top to bottom  $z_{\text{ice}} = 0.2 H, 0.6 H, 1.0 H, 1.4 H$  and  $1.8 H$ . Ice particles grow faster, and to larger sizes, the closer to the midplane the atmospheric ice line is.

In Fig. 6.2 the particle growth for different  $z_{\text{ice}}$  is shown. The mean ice particle size in terms of dimensionless friction time  $\langle \Omega \tau_f \rangle$  is shown as a function of time in units of  $\Omega^{-1}$ . The curves show, from top to bottom,  $z_{\text{ice}} = 0.2 H$  (black),  $0.6 H$  (violet),  $1.0 H$  (blue),  $1.4 H$  (red) and  $1.6 H$  (yellow). As is clear from the figure, the particles grow to larger sizes as the ice line is moved closer to the midplane. This effectively means that for ice lines closer to the midplane, i.e. a narrower condensation region, vapour particles can easier penetrate to the larger ice particles, thus causing growth also of the larger ice particles that tend to have positions close to the midplane. This can be compared to Fig. 5.2 in which the particle scale height  $H_p$  for different particle radii  $\Omega \tau_f$  can be seen. Small particles have a scale height comparable to the gas scale height  $H_{p,\text{small}} \approx H$ , whereas for larger particles  $H_{p,\text{large}} \ll H$ . Placing the ice line at a height larger than  $1 H$  is thus equivalent to saying that also the smallest particles tend to stay within the condensation zone. There is therefore very little material available for particle growth. The few particles that do move across the ice line and sublimate will mostly redistribute material among the particles at the border of the condensation zone. Growth in runs with  $z_{\text{ice}} \gtrsim 1 H$  is therefore both slow, and to modest particle sizes. However, some growth can still be seen, even for these runs. This suggests that, even without taking radial mixing into account, condensation plays a role also far from the radial ice line.

Placing the atmospheric ice line closer to the midplane than  $1 H$  and thus decreasing the distance between the ice line and the midplane means letting larger and larger particles traverse the ice line and sublimate. There is thus more material available for growth for the lucky few particles that manage to stay within the condensation zone. Thus, many small particles are sacrificed as a few large ice particles grow even larger.

## 6.2. ATMOSPHERIC ICE LINE

---

For all  $z_{\text{ice}} \leq 1 H$  a growth to  $\Omega\tau_f > 0.01$  is seen, equivalent to a growth of at least centimeter-sized pebbles. For  $z_{\text{ice}} = 0.6 H$  and  $z_{\text{ice}} = 0.2 H$  growth to decimeter- and meter-sized rocks and boulders, respectively, is found.

### 6.2.2 Varying the turbulent $\alpha$ -value

Simulations were run with different values of  $\alpha$  in order to test the influence of turbulence strength on the results. In Fig. 6.3 the mean particle size in dimensionless friction time  $\langle\Omega\tau_f\rangle$  is shown as a function of the height of the ice line above the midplane  $z_{\text{ice}}$ . The system is shown at  $t = 10\,000 \Omega^{-1}$ . The slightly varying shapes of the curves are interpreted as reflecting the fact that varying the  $\alpha$ -values and particle sizes influences the time it takes for the system to reach equilibrium. The full lines are modelled values, and the colours denote turbulence strength, with  $\alpha = 10^{-2}$  as blue,  $\alpha = 10^{-3}$  as red and  $\alpha = 10^{-4}$  as yellow.  $\alpha = 10^{-2}$  is the default turbulence strength used in the rest of this work, based on observations (Hartmann et al. 1998). As can be seen, reducing the strength of turbulence gives less growth. This is to be expected as the main effect of decreasing the level of turbulence is to lower the effective particle scale height, as this is set by an equilibrium between sedimentation and turbulent diffusion. As a comparison the analytical relation between mean particle size and particle scale height, in a system where vertical gravity and turbulent diffusion is dominating, is shown as dotted lines. As for the modelled values  $\alpha = 10^{-2}$  is shown as blue,  $\alpha = 10^{-3}$  as red and  $\alpha = 10^{-4}$  as yellow. The scale height of particles in terms of the gas scale height, from Eq. 2.41, is

$$\frac{H_p}{H} = \sqrt{\frac{\alpha}{\Omega\tau_f + \alpha}}. \quad (6.1)$$

Setting  $H_p \sim z_{\text{ice}}$  gives an analytical estimate of the corresponding particle size, shown in Fig. 6.3, as

$$\Omega\tau_f \sim \frac{\alpha}{(z_{\text{ice}}/H)^2} - \alpha \sim \alpha \left( \frac{1}{(z_{\text{ice}}/H)^2} - 1 \right). \quad (6.2)$$

The analytical expression underestimates the resulting  $\Omega\tau_f$ . The reason for this is that a certain  $z_{\text{ice}}$  in reality corresponds to a larger value than  $1 H_p$ , as the area below  $1 H_p$  does not include all particles (by definition, as it is the particle scale height). Therefore, a better estimate would be given by  $z_{\text{ice}} = c H_p$ , where  $c > 1$  is a constant. Nevertheless, already by using  $z_{\text{ice}} \sim H_p$  it is clear that the analytical and modelled curves follow similar slopes in the regions where applicable, i.e. for all particle sizes with  $H_p < H$ .

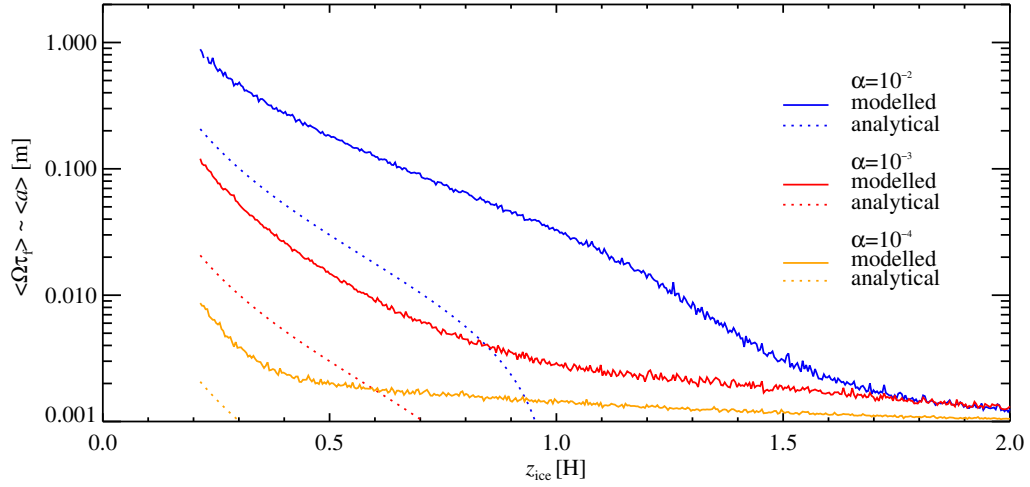


Figure 6.3: Ice particle growth dependence on strength of turbulence. The mean particle size in dimensionless friction time  $\langle \Omega \tau_f \rangle$  is shown as a function of the distance from the atmospheric ice line to the midplane  $z_{ice}$ , in gas scale heights  $H$ . The system is shown after  $10\,000\ \Omega^{-1}$ . Different colours denote different  $\alpha$ -values, blue is  $\alpha = 10^{-2}$ , red is  $\alpha = 10^{-3}$  and yellow is  $\alpha = 10^{-4}$ . Solid lines are modelled values and dotted lines are analytical values, set by Eq. 6.1. The modelled and analytical values follow the same slope in the applicable range.

### 6.3 Radial and atmospheric ice lines

Simulations were also done including both the radial and atmospheric ice lines, corresponding to placing the simulation domain at the position of the radial ice line. As also the radial direction becomes important when including the radial ice line, radial drift was included in these simulations.

### 6.3. RADIAL AND ATMOSPHERIC ICE LINES

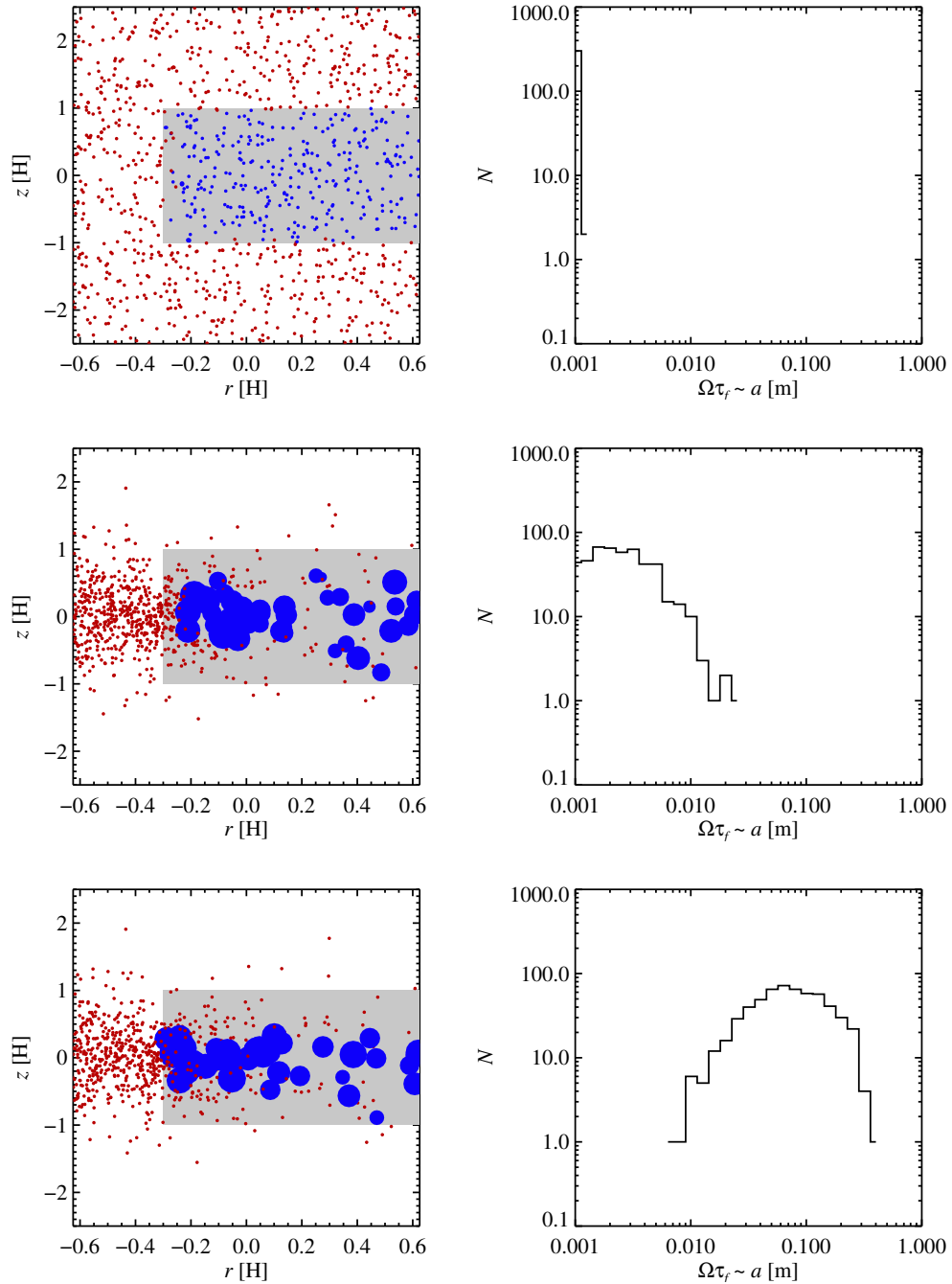


Figure 6.4: Left panels: Distribution of blue ice particles and red vapour particles, for  $t=0$ , 100 and  $1000 \Omega^{-1}$ , from top to bottom. The grey area corresponds to the condensation zone. The number of particles shown is inversely scaled with size for visibility. Right panels: Size distribution of ice particles, for  $t=0$ , 100 and  $1000 \Omega^{-1}$ .

Figure 6.4 shows the particle growth for a typical simulation with both radial and atmospheric ice line included. The system is shown at  $t = 0$ , 100 and  $1000 \Omega^{-1}$ , from top to bottom.

### 6.3. RADIAL AND ATMOSPHERIC ICE LINES

To the left the ice particles, shown in blue, and vapour, shown in red, are shown in the simulation box. For ice particles, the size of the blue dot is proportional to the logarithm of the physical radius of the ice particle. The number of particles shown in the figure is inversely scaled with particle radius. The grey region is the condensation region, enclosed by the radial and atmospheric ice lines. The right panels show the size distribution of the system.

The addition of the radial ice line gives a growth to larger sizes than in simulations including only the atmospheric ice line. Further, the size distribution is fairly narrow at all times, as the most important contribution to growth of large particles is given by the vapour coming in via the radial ice line. For all simulations made with the radial ice line included the strength of turbulence was kept fixed, at  $\alpha = 10^{-2}$ .

#### 6.3.1 Varying the atmospheric ice line position

With the radial ice line included, the position of the atmospheric ice line was varied, as can be seen in Fig. 6.5

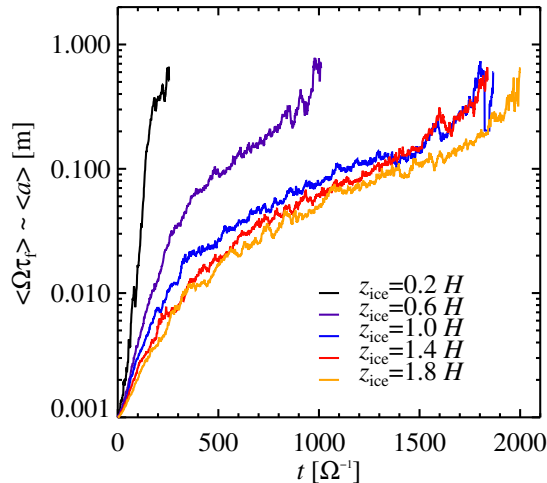


Figure 6.5: Particle growth dependence on atmospheric ice line position, for a simulation including both radial and atmospheric ice lines. The figure shows mean dimensionless friction time  $\langle \Omega \tau_f \rangle$  as a function of time in inverse Keplerian orbits  $\Omega^{-1}$ . The height of the atmospheric ice line above the midplane  $z_{\text{ice}}$  is denoted as: black  $0.2 H$ , violet  $0.6 H$ , blue  $1.0 H$ , red  $1.4 H$  and yellow  $1.8 H$ . The position of the radial ice line is at  $r_{\text{ice}} = -0.3 H$ , and the strength of turbulence is  $\alpha = 10^{-2}$ .

Fig. 6.5 shows how the mean particle size in dimensionless friction time  $\langle \Omega \tau_f \rangle$  as a function of time in  $\Omega^{-1}$  varies with atmospheric ice line position  $z_{\text{ice}}$ . The colours show different heights of the atmospheric ice line above the midplane, with black denoting  $z_{\text{ice}} = 0.2 H$ , violet  $z_{\text{ice}} = 0.6 H$ , blue  $z_{\text{ice}} = 1.0 H$ , red  $z_{\text{ice}} = 1.4 H$  and yellow  $z_{\text{ice}} = 1.8 H$ .

Three important effects can be seen. Firstly, as in previous sections, growth is faster for  $z_{\text{ice}}$  close to the midplane and slower for  $z_{\text{ice}}$  further away from it. As previously discussed,

### 6.3. RADIAL AND ATMOSPHERIC ICE LINES

this is due to the larger supply of material available for growth in a narrow condensation region, as compared to a wider condensation region. Secondly, for all  $z_{\text{ice}}$  a growth to large particle sizes  $\langle \Omega \tau_f \rangle \approx 1$  can be seen. Compared to simulations only including the atmospheric ice line, this is a substantial growth increase for all  $z_{\text{ice}}$ . The only exception is  $z_{\text{ice}} = 0.2H$  for which a large growth was found also without including the radial ice line. The growth increase can be explained by the fact that the inclusion of the radial ice line gives a way of supplying extra material to the growing ice particles. Importantly, the material supplied via the radial ice line has access directly to the large particles in the midplane, as opposed to the material supplied via the atmospheric ice lines. The last effect to be noted is that growth stops at  $\langle \Omega \tau_f \rangle \approx 1$  for all  $z_{\text{ice}}$ . This is due to the radial drift, which eventually removes all ice particles from the simulation. From Eq. 5.16 it can be seen that the radial drift inwards peaks for particles of  $\langle \Omega \tau_f \rangle \approx 1$ . As particles reach this size they thus drift inwards, past the radial ice line, and sublimate.

#### 6.3.2 Varying the simulation box size

To assess the importance of the size of the simulation domain, simulations were made where the box size was varied in the radial direction.

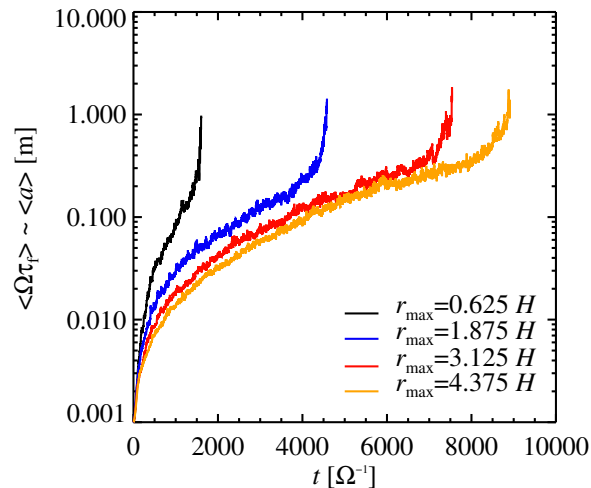


Figure 6.6: Particle growth for different radial sizes of the simulation box. The mean dimensionless friction time  $\langle \Omega \tau_f \rangle$  is shown as a function of time in inverse Keplerian orbits  $\Omega^{-1}$ . The size of the box has been extended in the radial direction, with  $r_{\text{max}}$  colour coded as: black  $0.625 H$ , blue  $1.875 H$ , red  $3.125 H$  and yellow  $4.375 H$ . For all runs  $z_{\text{min}} = -2.5 H$ ,  $z_{\text{max}} = 2.5 H$ ,  $r_{\text{min}} = -0.625 H$  and  $\alpha = 10^{-2}$ .

In Fig. 6.6 colours corresponds to different sizes of the simulation box, with black corresponding to the default box size  $r_{\text{max}} = 0.625 H$ , blue corresponds to  $r_{\text{max}} = 1.875 H$ , red to  $r_{\text{max}} = 3.125 H$  and yellow to  $r_{\text{max}} = 4.375 H$ . For all simulations  $r_{\text{min}} = -0.625 H$ ,  $r_{\text{ice}} = 0.3$  and  $z_{\text{ice}} = 1H$  have been kept fixed. The number of particles has been increased with the box size so that the particle number density is equal for all simulations. For all box sizes the radial drift causes the simulation domain to become completely depleted in ice particles as sizes of  $\langle \Omega \tau_f \rangle \approx 1$  are reached. The time it takes before this happens varies with box size, as

the growth time scale increases approximately linearly with the size of the simulation domain. The reason for this is that the radial ice line, which is responsible for the fastest growth, plays a less prominent role for larger box sizes, as material is spread over a larger radial extent.

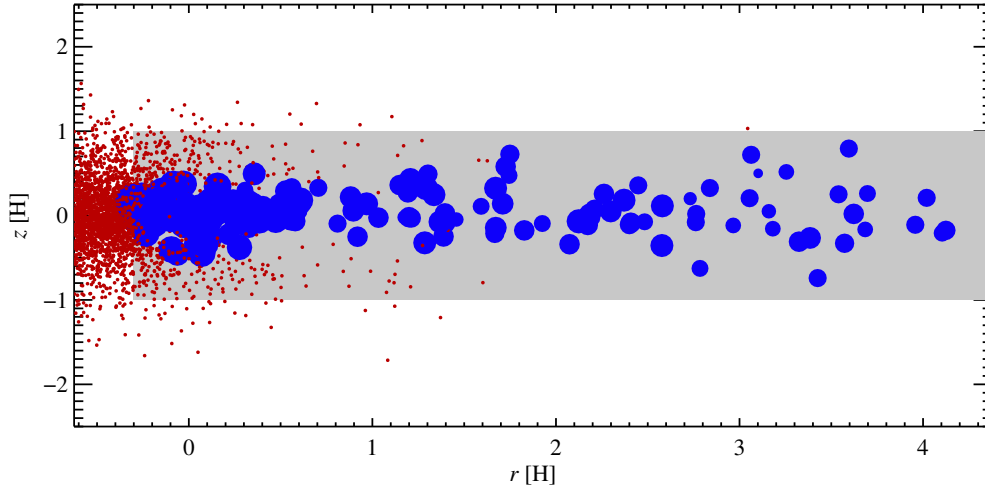


Figure 6.7: State of the system in Fig. 6.6 with  $r_{\max} = 4.375$  after  $t = 5\,000\,\Omega^{-1}$ . Particles grow significantly everywhere at all  $r > r_{\text{ice}}$ , with the largest growth close to the radial ice line.

Fig. 6.7 shows the state of the largest simulation box ( $r_{\max} = 4.375$ ) after  $t = 5\,000\,\Omega^{-1}$ . Although the radial ice line is most important for growth to the largest particle sizes, particles experience significant growth even at large  $r$ .

## 6.4 Simulations including a pressure variation

Including the radial ice line in the simulations, as in previous section, make ice particles radially drift inwards across the ice line and sublimate. This is a problem as it constrains the particle growth, and depletes the region of already grown particles. However, introducing pressure variations in the model naturally leads to trapping of particles in so-called pressure bumps, or regions of higher pressure (Whipple 1972). Particles move along pressure gradients. In the simplest possible protoplanetary disc, this corresponds to a motion radially inwards. However, a realistic disc has variations in the pressure gradient, leading to local pressure maxima and minima. This makes it possible to trap particles in these pressure maxima, as shown in Fig. 6.8.

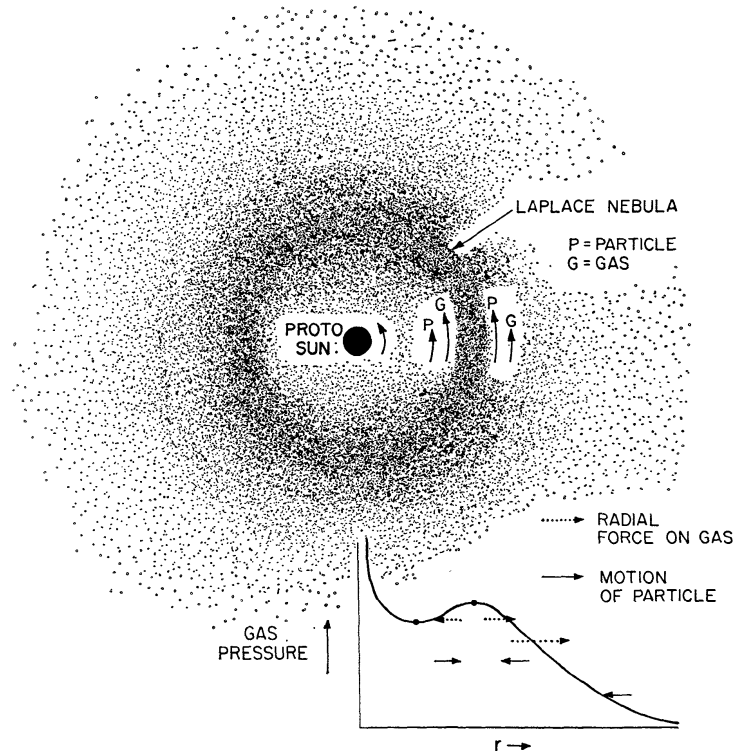


Figure 6.8: Illustration of particle trapping in a pressure bump. The protoplanetary disc, seen from above, is marked as the “Laplace nebula”, showing gas and particles orbiting the central star. In the lower right corner the gas pressure as a function of radial distance from the star is shown. Particle motions are shown as full arrows and the radial force on the gas as dotted arrows. Particles follow the pressure gradient and end up at the position of the local pressure maximum, called the pressure bump. Figure from Whipple (1972).

Such pressure variations arise spontaneously in simulations of protoplanetary discs (see e.g. Johansen et al. (2009a) ) where turbulence is driven by the magnetorotational instability, an instability in which Keplerian flows are unstabilised in the presence of moderate magnetic fields (Balbus & Hawley 1991). However, the rapid change of dust density at the ice line also lead to local radial maxima of gas column density  $\Sigma$  and pressure  $P$ . Just as the overall radial pressure gradient in the disc makes particles drift inwards due to the gas headwind, a local pressure maximum causes particles to move towards the local maxima. Particles move in the direction of the pressure gradient and thus get trapped in the pressure bump, located just outwards of the ice line (Kretke & Lin 2007).

In these simulations the simplest possible form of a pressure bump was inserted into the model, by setting the systematic radial velocity to  $r_{\text{rd}} = 0$  in a region just outwards of the radial ice line.

## 6.4.1 Varying the atmospheric ice line position

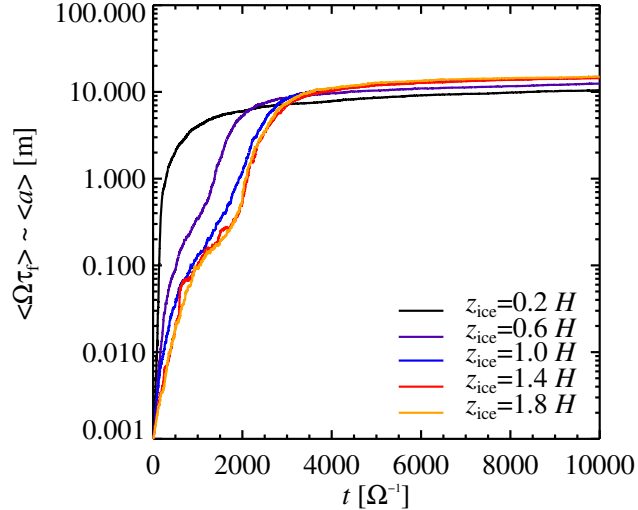


Figure 6.9: Particle growth with an added pressure bump. The mean dimensionless friction time  $\langle \Omega \tau_f \rangle$  is shown as a function of time in inverse Keplerian orbits  $\Omega^{-1}$  for different atmospheric ice line height above the midplane. The radial drift velocity is  $v_r = 0$  at  $r_{\text{ice}} \leq r \leq (r_{\text{ice}} + H)$ , mimicking a pressure bump. The position of the radial ice line is at  $r_{\text{ice}} = -0.3 H$  and the position of the atmospheric ice line  $z_{\text{ice}}$  is denoted as: black  $0.2 H$ , violet  $0.6 H$ , blue  $1.0 H$ , red  $1.4 H$  and yellow  $1.8 H$ . In all runs  $\alpha = 10^{-2}$ .

Fig. 6.9 shows how the mean particle size varies with atmospheric ice line position  $z_{\text{ice}}$ . The height of the atmospheric ice line is denoted by different colours, where black denotes  $z_{\text{ice}} = 0.2 H$ , violet  $z_{\text{ice}} = 0.6 H$ , blue  $z_{\text{ice}} = 1.0 H$ , red  $z_{\text{ice}} = 1.4 H$  and yellow  $1.8 H$ . The radial ice line is kept fixed at  $r_{\text{ice}} = -0.3 H$ . The effect of inserting a pressure bump is clearly visible in Fig. 6.9, in that the simulation domain now does not get depleted in ice particles. Instead, particles grow to much larger sizes,  $\langle \Omega \tau_f \rangle \approx 10$ , for all  $z_{\text{ice}}$ . A tendency towards larger  $z_{\text{ice}}$  giving larger final particle sizes, in contrast to all simulations in previous sections, can be seen. This is explained by the fact that the growth by vapour coming in via the radial ice line is more important for large  $z_{\text{ice}}$  than for small. For a narrow condensation zone most of the growth happens early in the simulation, via the atmospheric ice line, binding more of the mass into the midplane layer early on. For large  $z_{\text{ice}}$  more mass is free, i.e. in the form of small ice particles which can easily be converted to vapour, to take part in the growth via the radial ice line. This growth is more efficient at giving large particles, as mass can here be injected directly into the midplane layer, where the largest particles reside, as shown in Fig. 6.10.

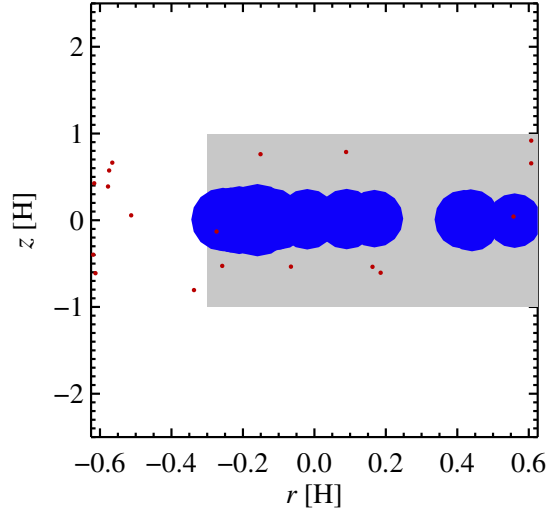


Figure 6.10: State of simulation domain with added pressure bump at  $t = 5000 \Omega^{-1}$ . The system is equivalent to that in Fig. 6.9 with  $z_{\text{ice}} = 1 H$ . Particles grow large enough to become insensitive to turbulence, giving a midplane layer of immobile  $\Omega\tau_f \approx 10$  particles. The particles are concentrated towards the radial ice line, trapped inside the pressure bump region.

#### 6.4.2 Varying the simulation box size

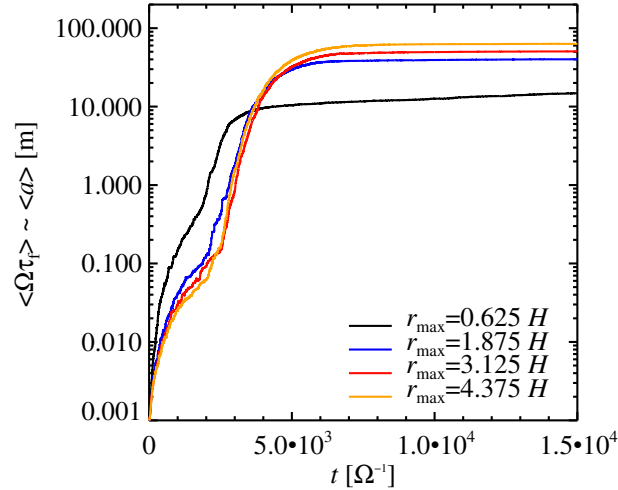


Figure 6.11: Particle growth with an added pressure bump for a simulation box that has been extended in the radial direction. The mean dimensionless friction time  $\langle \Omega\tau_f \rangle$  is shown as a function of time in inverse Keplerian orbits  $\Omega^{-1}$ . The radial extension of the box is colour coded, showing  $r_{\text{max}}$  as: black  $0.625 H$ , blue  $1.875 H$ , red  $3.125 H$  and yellow  $4.375 H$ . For all runs  $z_{\text{min}} = -2.5 H$ ,  $z_{\text{max}} = 2.5 H$ ,  $r_{\text{min}} = -0.625 H$  and  $\alpha = 10^{-2}$ .

#### 6.4. SIMULATIONS INCLUDING A PRESSURE VARIATION

---

In Fig. 6.11 the size of the simulation box has been varied, whereas  $r_{\text{ice}} = -0.3$  and  $z_{\text{ice}} = 1 H$  have been kept fixed. The different box sizes are denoted by colours as follows: black denotes  $r_{\text{max}} = 0.625 H$ , blue  $r_{\text{max}} = 1.875 H$ , red  $r_{\text{max}} = 3.125 H$  and yellow  $r_{\text{max}} = 4.375 H$ . In all runs  $r_{\text{min}} = -0.625 H$  and the radial drift velocity is  $v_r = 0$  at  $r_{\text{ice}} \leq r \leq (r_{\text{ice}} + H)$ . The number of particles has been increased so that the particle number density is equal for all box sizes. The large growth is explained by the fact that all ice particles eventually are trapped inside the pressure bump, where they grow until all available mass has condensed on to them. A larger simulation box gives growth to larger particle sizes, as this implies a larger total mass included in the simulation.

#### 6.4. SIMULATIONS INCLUDING A PRESSURE VARIATION

---

# Chapter 7

## Discussion

### 7.1 General assumptions and simplifications

This model has been developed primarily to investigate the water ice line at  $r \approx 3$  AU. However, similar ice lines, or condensation fronts, exist also for other chemical species, and as this model is scalable to any  $r$  it can easily be adapted to include any condensation front. Of importance for planet formation purposes are in particular the ammonia, methane, carbon monoxide and molecular nitrogen ice lines further out in the protoplanetary disc, and the numerous silicate ice lines further in towards the central star. A global disc model, including all ice lines of the most important chemical species in the protoplanetary disc, would be an interesting extension of this work.

The particles in this model are very simplified compared to real dust grains in a protoplanetary disc. The composition is assumed to be water ice only, furthermore there is no variation in neither material nor porosity, both of which matter for growth. The particles are also assumed to be perfectly spherical.

The systematic motion of gas accretion onto the central star has been ignored in this work. However, compared to the time scales we are interested in the accretion process is slow enough to be safely neglected (Hartmann et al. 1998).

The ice line has throughout this work been considered as fixed. Seen over the life time of the disc this is not true, as the ice line probably moves both in a systematic way over long time scales and due to shorter heating events (Armitage 2011). However, as the time scale for growth by condensation found in this work is on the order of  $\tau \approx 1000 \Omega^{-1}$ , which is very short compared to the life time of the disc  $\tau_{\text{disc}} \approx 1$  Myr, we find it safe to consider a fixed ice line.

### 7.2 Particle structure

In this model the ice particles are modelled as one-component particles; homogeneous water ice particles. In reality these particles would have a (at least) two-component composition, that of a rocky core and an ice mantle. This is due to the fact that supersaturated water vapour is needed for homogeneous nucleation, i.e. for the spontaneous formation of a new

## 7.2. PARTICLE STRUCTURE

---

ice particle. As this is typically not the case in the conditions prevailing in a protoplanetary disc, water vapour instead condenses onto an existing grain, either a rocky dust particle, or a particle with an already existing ice layer on top of the dust grain. Whether vapour preferably condenses onto a bare dust grain or an ice particle depends on material properties and on their respective sizes.

Ignoring the small dust particles inside the ice in this model possibly leads to an over-estimation of the growth of the larger ice particles, since the vapour would condense onto the small dust particles instead of the larger ice particles. This is based on the fact that for a fixed amount of mass, the smaller dust particles have a larger combined surface area than the larger particles, and therefore the probability that a vapour particle condenses onto a smaller dust particle than onto a larger particle. This is for the case when the material properties of the dust and the ice are such that an equally large dust and ice particle has equal probability of having a vapour particle condensing onto them.

This means that instead of growth of a few large ice particles that sediment towards the midplane and thereby are protected against sublimation, there would be a continuous sublimation and condensation of the small ice particles at the ice line. This effect can already be seen in the model, as small particles are more likely to cross the ice line and sublimate, and conversely, to grow by condensation, but would be amplified by the introduction of a dust core.

Material effects might make this problem more severe. The dust grain composition is assumed to be similar to that of interstellar dust grains, either being pure interstellar dust grains or conglomerates thereof. This gives us the most important dust species as silicates and carbonaceous material, with silicates typically assumed to be the dominating one (Draine 2003). Silicates have material properties that makes them more efficient as ice nuclei than water ice particles, with the relative energy for water adsorption onto a silicate (forsterite) grain being approximately  $-1\,000\text{ kJ mol}^{-1}$  (Goumans et al. 2009). This means that the effect of small particle growth at the expense of the larger ones is amplified when taking the material properties into account .

There are however a number of possible solutions to this problem, in terms of possible reasons for the vapour to condense onto ice particles instead of the small dust grains. Firstly, the dust grains are not likely to all have the same size. Rather, they would have a size distribution where the smallest grains can be nanometer-sized (Draine 2003). The largest dust particles of relevance are the ones of the largest size that are strongly enough coupled to the gas to be present at the relevant vertical distance from the midplane. This is around micrometer-scale (see Fig. 5.3). The Kelvin curvature effect states that the equilibrium vapour density for a curved surface is higher than for a flat surface, meaning that vapour more easily condenses onto a flat surface than a curved one, an effect which is most important for the smallest particles, around nanometer-sizes (Sirono 2011). Therefore vapour will always prefer condensing onto the larger particles, leaving the smallest ones as bare dust grains.

Secondly, small grains are likely to be hotter than larger particles, making it less likely that the water vapour condenses onto them. The temperature of the grains are set by the balance between absorption and emission efficiency. As grains absorb and emit radiation most efficiently in wavelengths smaller than and up to their own size there is a size-dependent effect.

### 7.3. PARTICLE COLLISIONS

---

The spectral energy distribution of a solar-type star peaks at wavelengths of about  $1\ \mu\text{m}$ . All grains of this size and larger therefore absorb incoming radiation with approximately equal efficiency. However, grains emit in infra-red wavelengths (larger than  $1\ \mu\text{m}$ ), the larger grains can thus emit more energy than the smaller ones (since any grain can only emit in wavelengths up to its own size). The resulting temperature for the smaller grains is therefore higher than for the larger grains (Krivov et al. 2008; Vitense et al. 2012). This mechanism is only valid if the grains reside in the atmosphere of the disc, where it is optically thin to the stellar radiation. For grains deeper in the disc the absorbed energy will be the re-emitted infra-red radiation from neighbouring grains, and no temperature difference between small and large grains will result.

Further, there is a possibility that material effects might prevent water vapour from condensing onto the dust grains. As mentioned above, bare silicate grains are more efficient as ice nuclei than ice-covered ones. However, for carbonaceous grains the opposite is true (Papoular 2005), meaning that vapour condenses more easily onto a water ice particle than onto a bare carbonaceous grain. For a grain population with ice coated particles and bare carbonaceous grains, the carbonaceous grain would therefore be left bare, whereas the ice grains would continue growing.

Finally, even though water vapour prefers to condense onto dust grains, turbulent mixing throughout the disc would still lead to significant particle growth. The small dust grains originating from sublimated ice particles close to the water ice line will be transported with the turbulence both towards and from the central star. The dust grains having a net inwards motion will eventually move close to the silicate ice line, where they can grow by vaporized silicates condensing onto them. If transported back towards the water ice line they have thus grown, and the size effect of the silicate grains being smaller than the ice particles is less important.

### 7.3 Particle collisions

Throughout this work, collisions between particles have been neglected. A full treatment of particle collisions is far beyond the scope of this work, but with simple arguments it can be shown that including particle collisions most likely would not inhibit, but possibly increase, the particle growth.

In order to estimate whether particle collisions are important, the collision time scale  $\tau_c$  is compared to the growth time scale  $\tau_g$  found from simulations. The collision time scale is

$$\tau_c = \frac{\lambda_p}{v}, \quad (7.1)$$

where  $\lambda_p$  is the mean free path of the particles and  $v$  is the typical relative particle velocity. The mean free path is calculated from the particle number density  $n_p$  and the collisional cross section  $\sigma_p$ . Assuming all particles are spherical and of the same size, the collision time scale can be written as

$$\tau_c = \frac{m}{v\rho_p\pi(2a)^2}. \quad (7.2)$$

### 7.3. PARTICLE COLLISIONS

Expressing the particle mass in terms of radius,  $m = (4/3)\pi a^3 \rho_\bullet$ , gives

$$\tau_c = \frac{1}{3} \frac{\rho_\bullet a}{\rho_p v}, \quad (7.3)$$

where  $a$  can be expressed in terms of friction time (see Eq. 2.7), giving

$$\Omega \tau_c = \frac{1}{3} \frac{\rho_g c_s}{\rho_p v} \Omega \tau_f, \quad (7.4)$$

where the time scales have been non-dimensionalized. The typical particle density in the disc is  $\rho_p/\rho_g \approx 0.01$  (Hayashi 1981) and the typical turbulent relative velocity between two particles of equal size is given by

$$v = \frac{3}{2} \sqrt{\Omega \tau_f \alpha c_s} \quad (7.5)$$

(Weidenschilling 1984), with  $\alpha = 10^{-2}$ . With the velocity from Eq. 7.5, the particle time scale as a function of particle size can be expressed as

$$\Omega \tau_c = \frac{2}{9} \frac{1}{0.01} \sqrt{\frac{\Omega \tau_f}{\alpha}}. \quad (7.6)$$

The particle collision time scale as a function of particle size is plotted in Fig. 7.1.

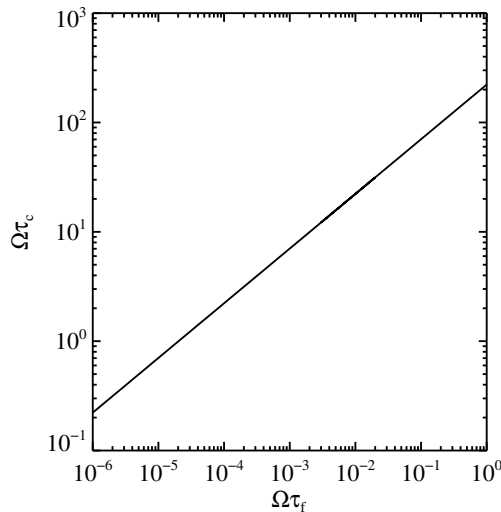


Figure 7.1: Dimensionless collision time scale as a function of particle size in dimensionless friction time. The collision time scale decreases linearly with particle size. Ice particles are in the size range  $10^{-3} \lesssim \Omega \tau_f \lesssim 1$ , whereas the refractory core contained inside an ice particle is smaller,  $a_{\text{dust}} \approx 1 \mu\text{m}$ .

In particular, the smallest particles included in this simulation, with  $\Omega \tau_f = 10^{-3}$ , have a collision time scale of  $\tau_{c,\text{small}} \approx 10 \Omega^{-1}$  and large particles with  $\Omega \tau_f = 1$  have  $\tau_{c,\text{large}} \approx 100 \Omega^{-1}$ . Comparing these numbers to the growth time scale from the simulations  $\tau_g \approx 1000 \Omega^{-1}$ , it can be seen that collisions between large particles can be neglected, whereas for smaller

particles collisions become increasingly important. Evidently, a large particle has grown from a small one, so that during its lifetime a particle does experience a significant number of collisions. However, as is argued in the following, only collisions between large particles are destructive. Therefore also collisions between small particles can be neglected, as they do not inhibit growth even though they do happen frequently.

In general, small particles tend to stick together to a larger extent than large particles, if colliding, whereas larger particles are more prone to bouncing or fragmenting. Collisions amongst large particles would therefore have a tendency to be destructive, whereas small-particle collisions are more likely to favour growth (or at least not counteract it). For silicate particles growth via collisions involving equal-sized particles is very difficult beyond millimeters, however collisional growth involving small particles colliding with a large target is possible, although slow (Windmark et al. 2012). Ice particles have an increased stickiness compared to rocky particles, making small particle growth, and in particular growth involving different-sized particles, more likely for ice than for dust particles (Bridges et al. 1996). It has also been suggested that colliding ice particles stick together due to collisional fusion, i.e. by collisional melting and the subsequent fusion of the particles (Wettlaufer 2010). Taking particle collisions into account in our simulations would therefore most probably lead to an increased particle growth and not the opposite.

An important implication of collisions is that it provides a natural means of removing small dust grains released from the ice particles when sublimating. As these dust grains are very efficient ice nuclei, they might prevent growth of already large particles by “stealing” all the vapour. However, as these dust grains are even smaller than the smallest ice particles,  $a_{\text{dust}} \approx 1\mu\text{m}$ , the collision time scale is very short. Although the time scale for small and large particles colliding is not calculated here, a likely scenario is that the  $\mu\text{m}$ -sized dust grains are swept up by larger ice particles. This does not increase the growth significantly, but has the important benefit that the small dust grains are removed so that vapour has to condense onto growing ice particles.

## 7.4 Connection to observations

The existence of an atmospheric ice line was inferred by Meijerink et al. (2009), leading to what the authors call a “vertical cold finger effect”. The authors suggest that this effect can explain their observations of less water vapour than expected in protoplanetary discs. Our work is completely in line with that of Meijerink et al. (2009), and can be seen as an extension of their discussion.

Observations with Herschel space observatory of cold water vapour in a protoplanetary disc has further established the importance of the ice line, both the radial and atmospheric sections of it (Hogerheijde et al. 2011). Their work confirms water vapour freeze-out at radial distances larger than the ice line as being the best explanation for the observed lack of water vapour at large radial distances.

Further support for this idea comes from observations of the CO ice line, which has been resolved in one Herbig Ae disc (HD 163296) by Qi et al. (2011). A sharp drop in CO abundance was detected at a radial distance of 155 AU from the star, where the midplane temperature is

#### 7.4. CONNECTION TO OBSERVATIONS

---

19 K. This shows a freeze-out of CO onto midplane grains outwards of the CO ice line. The fact that some CO could still be detected outwards of this CO ice line shows that the vertical structure of the disc is important, with an outer layer that still holds CO in gaseous form.

Our model indeed predicts a freeze-out of water vapour outside of the radial ice line, as found tentatively from observations and suggested by Meijerink et al. (2009). The mechanism we suggest is by condensation and subsequent sedimentation of large particles.

## Chapter 8

# Conclusions

From the results obtained in this project it is clear that condensation is an important ice particle growth mechanism that needs to be taken into account in models of early planet formation. As the more thoroughly investigated mechanism of coagulation seems incapable of forming particles larger than centimeters, growth by condensation is an important alternative or complementary mechanism.

Starting from particles of size  $\langle \Omega \tau_f \rangle = 10^{-3}$ , particles grow to up to  $\langle \Omega \tau_f \rangle \approx 1$  on a time scale of  $t = 1\,000 \Omega^{-1}$  and with a turbulence of  $\alpha = 10^{-2}$ . This corresponds to a growth from millimeter- to meter-sized particles in 1 000 yr at  $r \approx 3\text{AU}$  where the water ice line is located. A turbulent  $\alpha$ -value of  $10^{-2}$  corresponds to the strength of turbulence that have been inferred from observations of protoplanetary discs.

Introducing pressure variations in the system even causes growth to  $a > 1$  m. These particles are large enough to have passed the size for which the radial drift inwards is the largest,  $a \approx 1$  m. As the particles therefore are not lost to the central star via radial drift, they can grow further by other mechanisms, towards planets.

Most importantly, even a growth from millimeter- to decimeter-sized particles is a significant step. This means that the particles are large enough to take part in dynamical instabilities, such as the streaming instability where particles clump together, thereby causing further growth into planetesimals, as shown in Fig. 8.1. Further growth from planetesimals to planets is possible via gravitational interactions.

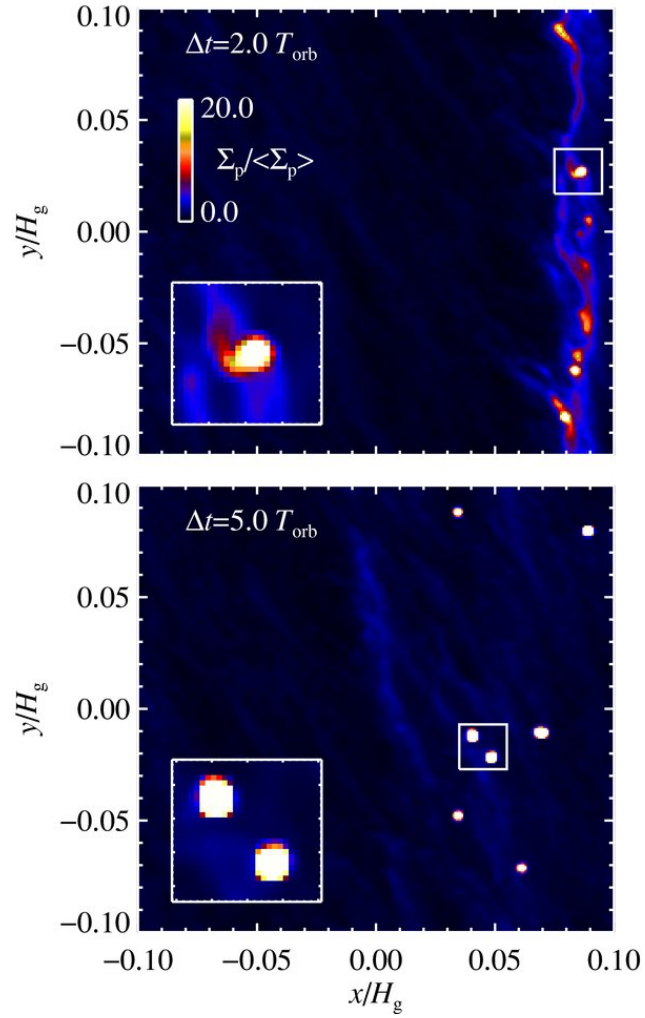


Figure 8.1: Planetesimal formation via streaming instability from computer simulation by Johansen et al. (2009b). The upper panel shows a growing dense particle filament, formed by streaming instability and self-gravity. The particles are of centimeter- to decimeter-sizes, which is the particle size most easily formed by condensation. The inlay figure shows an accreting clump of particles. In the lower panel the material has formed 7 gravitationally bound clumps, each containing the mass equivalent of a 100-200 km scale planetesimal. Density is colour-coded, with dark colours showing low-density regions, and bright colours high-density regions. Length-scales are given in gas scale heights and time-scales in orbits.

## Appendix A

# From random walk to the diffusion coefficient

The code used is two-dimensional, but as the mathematics is the same for 1D and 2D, the diffusion coefficient for 1D is derived here, for simplicity. Starting from a one-dimensional grid with equidistant grid-points the probability  $P(i, N)$  to be at location  $i$  after  $N$  steps can be expressed as

$$P(i, N) = \frac{1}{2}P(i-1, N-1) + \frac{1}{2}P(i+1, N-1). \quad (\text{A.1})$$

meaning that if a particle is found at grid point  $i$  after  $N$  steps, it must have come from either point  $i-1$  or point  $i+1$ , with a 50% probability to have been at point  $i-1$  after  $N-1$  steps, and an equal probability to have been at point  $i+1$  after  $N-1$  steps. With  $t = N\tau$  and  $x = il$  Eq. A.1 can be rewritten as

$$P\left(\frac{x}{l}, \frac{t}{\tau}\right) = \frac{1}{2}P\left(\frac{x}{l} - l, \frac{t}{\tau} - \tau\right) + \frac{1}{2}P\left(\frac{x}{l} + l, \frac{t}{\tau} - \tau\right) \quad (\text{A.2})$$

Since the probability is independent of length- and timescales, Eq. A.2 can be multiplied with  $l$  and  $t$  to obtain

$$P(x, t) = \frac{1}{2}P(x-l, t-\tau) + \frac{1}{2}P(x+l, t-\tau). \quad (\text{A.3})$$

By definition, the derivative of  $P(x, t)$  with respect to  $t$ , as  $\tau \rightarrow 0$ , is

$$\frac{\partial P(x, t)}{\partial t} = \frac{P(x, t) - P(x, t-\tau)}{\tau}. \quad (\text{A.4})$$

Inserting Eq. A.3 in Eq. A.4 gives

$$\frac{\partial P(x, t)}{\partial t} = \frac{1}{2\tau} (P(x-l, t-\tau) + P(x+l, t-\tau) - 2P(x, t-\tau)). \quad (\text{A.5})$$

---

A second order Taylor expansion of Eq. A.5 about  $x$  and  $t$  with, respectively,  $\pm l$  and  $\tau$  as deviation gives

$$\begin{aligned} \frac{\partial P(x, t)}{\partial t} \approx \frac{1}{2\tau} & \left[ P(x, t) - l \frac{\partial P(x, t)}{\partial x} - \tau \frac{\partial P(x, t)}{\partial t} + \frac{l^2}{2} \frac{\partial^2 P(x, t)}{\partial x^2} + \frac{\tau^2}{2} \frac{\partial^2 P(x, t)}{\partial t^2} \right. \\ & + P(x, t) + l \frac{\partial P(x, t)}{\partial x} - \tau \frac{\partial P(x, t)}{\partial t} + \frac{l^2}{2} \frac{\partial^2 P(x, t)}{\partial x^2} + \frac{\tau^2}{2} \frac{\partial^2 P(x, t)}{\partial t^2} \\ & \left. - 2 \left( P(x, t) - \tau \frac{\partial P(x, t)}{\partial t} + \frac{\tau^2}{2} \frac{\partial^2 P(x, t)}{\partial t^2} \right) \right]. \end{aligned} \quad (\text{A.6})$$

Simplifying Eq. A.6 by cancelling terms gives

$$\frac{\partial P(x, t)}{\partial t} = \frac{l^2}{2\tau} \frac{\partial^2 P(x, t)}{\partial x^2} \quad (\text{A.7})$$

which is the diffusion equation in 1D with the diffusion coefficient

$$D_{1\text{D}} = \frac{l^2}{2\tau}. \quad (\text{A.8})$$

The diffusion coefficients for 2 and 3 dimensions can be found from equivalent arguments, giving the diffusion coefficients for 2D and 3D as

$$D_{2\text{D}} = \frac{l^2}{4\tau} \quad \text{and} \quad (\text{A.9})$$

$$D_{3\text{D}} = \frac{l^2}{6\tau}. \quad (\text{A.10})$$

# Bibliography

- Alexander, R. D., Clarke, C. J., & Pringle, J. E. 2006, MNRAS, 369, 229
- Andrews, S. M. & Williams, J. P. 2005, ApJ, 631, 1134
- Armitage, P. J. 2011, ARA&A, 49, 195
- Balbus, S. A. & Hawley, J. F. 1991, ApJ, 376, 214
- Beckwith, S. V. W., Sargent, A. I., Chini, R. S., & Guesten, R. 1990, AJ, 99, 924
- Blum, J. & Wurm, G. 2008, ARA&A, 46, 21
- Boss, A. P. 2003, ApJ, 599, 577
- Brauer, F., Dullemond, C. P., & Henning, T. 2008, A&A, 480, 859
- Bridges, F. G., Supulver, K. D., Lin, D. N. C., Knight, R., & Zafra, M. 1996, Icarus, 123, 422
- Davis, S. S. 2007, ApJ, 660, 1580
- Draine, B. T. 2003, ARAA, 41, 241
- Dullemond, C. P., Hollenbach, D., Kamp, I., & D'Alessio, P. 2007, Protostars and Planets V, 555
- Goumans, T. P. M., Catlow, C. R. A., Brown, W. A., Kästner, J., & Sherwood, P. 2009, Physical Chemistry Chemical Physics (Incorporating Faraday Transactions), 11, 5431
- Haisch, Jr., K. E., Lada, E. A., & Lada, C. J. 2001, ApJ, 553, L153
- Hartmann, L., Calvet, N., Gullbring, E., & D'Alessio, P. 1998, ApJ, 495, 385
- Hayashi, C. 1981, Progress of Theoretical Physics Supplement, 70, 35
- Haynes, D. R., Tro, N. J., & George, S. M. 1992, Journal of Physical Chemistry, 96, 8502
- Hogerheijde, M. 1998, PhD thesis, Department of Astronomy, University of California
- Hogerheijde, M. R., Bergin, E. A., Brinch, C., et al. 2011, Science, 334, 338
- Johansen, A. & Klahr, H. 2005, ApJ, 634, 1353
- Johansen, A. & Youdin, A. 2007, ApJ, 662, 627

## BIBLIOGRAPHY

---

- Johansen, A., Youdin, A., & Klahr, H. 2009a, *ApJ*, 697, 1269
- Johansen, A., Youdin, A., & Mac Low, M. 2009b, *ApJ*, 704, L75
- Kraus, A. L. & Ireland, M. J. 2012, *ApJ*, 745, 5
- Kretke, K. A. & Lin, D. N. C. 2007, *ApJ*, 664, L55
- Krivov, A. V., Müller, S., Löhne, T., & Mutschke, H. 2008, *ApJ*, 687, 608
- Lodders, K. 2003, *ApJ*, 591, 1220
- Meijerink, R., Pontoppidan, K. M., Blake, G. A., Poelman, D. R., & Dullemond, C. P. 2009, *ApJ*, 704, 1471
- Nakagawa, Y., Sekiya, M., & Hayashi, C. 1986, *Icarus*, 67, 375
- Papoular, R. 2005, *MNRAS*, 362, 489
- Qi, C., D'Alessio, P., Öberg, K. I., et al. 2011, *ApJ*, 740, 84
- Safronov, V. S. 1969, *Evolutsiia doplanetnogo oblaka.*, ed. Safronov, V. S.
- Shakura, N. I. & Sunyaev, R. A. 1973, *A&A*, 24, 337
- Shu, F. H., Adams, F. C., & Lizano, S. 1987, *ARA&A*, 25, 23
- Sirono, S.-i. 2011, *ApJ*, 735, 131
- Supulver, K. D. & Lin, D. N. C. 2000, *Icarus*, 146, 525
- Vitense, C., Krivov, A. V., Kobayashi, H., & Löhne, T. 2012, *A&A*, 540, A30
- Weidenschilling, S. J. 1977, *MNRAS*, 180, 57
- Weidenschilling, S. J. 1984, *Icarus*, 60, 553
- Wettlaufer, J. S. 2010, *ApJ*, 719, 540
- Whipple, F. L. 1972, in *From Plasma to Planet*, ed. A. Elvius, 211
- Wilner, D. J., D'Alessio, P., Calvet, N., Claussen, M. J., & Hartmann, L. 2005, *ApJ*, 626, L109
- Windmark, F., Birnstiel, T., Güttler, C., et al. 2012, *A&A*, 540, A73
- Youdin, A. N. & Lithwick, Y. 2007, *Icarus*, 192, 588
- Zsom, A. & Dullemond, C. P. 2008, *A&A*, 489, 931